

Chemical-structural modularity in the tetradymite group: A HRTEM study

CRISTIANA LIANA CIOBANU,^{1,2,*} ALLAN PRING,^{1,2} NIGEL JOHN COOK,³ PETER SELF,⁴
DAVID JEFFERSON,⁵ GABRIEL IONEL DIMA,⁶ AND VOLODYMYR MELNIKOVA⁷

¹South Australian Museum, North Terrace, Adelaide, S.A. 5000, Australia

²Department of Earth and Environmental Sciences, University of Adelaide, S.A. 5005, Australia

³Natural History Museum, University of Oslo, Boks 1172 Blindern, N-0318 Oslo, Norway

⁴Adelaide Microscopy, University of Adelaide, Frome Road, Adelaide, S.A. 5005, Australia

⁵Department of Chemistry, Cambridge University, Lensfield Road, Cambridge, CB2 1EW, U.K.

⁶Robinson College, Cambridge University, Grange Road, Cambridge, CB3 9AN, U.K.

⁷Institute of Geochemistry, Mineralogy and Ore Formation, NAS of Ukraine, Ky'iv, Ukraine

ABSTRACT

Mixed-layer compounds from the tetradymite group, in the range $\text{Bi}_2\text{Te}_3\text{-Bi}_8\text{Te}_3$, were studied by HRTEM. The formula $S'(\text{Bi}_{2k}\text{X}_3) \cdot L'[\text{Bi}_{2(k+1)}\text{X}_3]$ ($X = \text{chalcogen}$; S' , $L' = \text{number of short and long modules, respectively}$) was introduced as a working model. Diffraction patterns show that all phases are N -fold ($N = \text{layers in the stacking sequence}$) superstructures of a rhombohedral subcell with $c/3 = d_1 \sim 0.2 \text{ nm}$. The patterns, with two brightest reflections about the middle of d_1^* , are described by monotonic decrease of two modulations with increase in Bi: (1) $\mathbf{q} = \gamma \mathbf{c}_{\text{sub}}^*$ ($q \sim \text{homoatomic interval}$; $\gamma = 1.8\text{--}1.64$ for analytical range; $c_{\text{sub}} \sim 3d_1$), based on displacive modulation between chalcogen and Bi atoms; and (2) $\mathbf{q}_F = \gamma_F \mathbf{c}_{\text{sub}}^*$; $q_F = (i/N)d_1^* = id_N^*$, $i = S' + L'$, relating changes in module size and number to displacements in a basic substructure.

The \mathbf{q}_F model, besides underpinning the stacking sequences, was adapted to incorporate the homology for S' , L' modules related by k . The displacements are quantifiable by fractional shifts between reflections in the derived and basic structures. The condition for “the brightest two reflections about the middle of d_1^* to be separated by id_N^* ” is fulfilled only if the shift at this position is minimal (equal to $1/N_b$; $N_b = \text{layers in the basic structure}$). This model and accompanying program compiled to find suitable N_b and simulate intensity pattern(s) can be used to (1) constrain stacking sequences estimated from observation; (2) predict polysomes as larger building blocks; and (3) discriminate single-phases from random polysomes.

The formula $n\text{Bi}_2 \cdot m\text{Bi}_2\text{X}_3$ describing the configuration for Bi_{2k}X_3 modules by $n/m = k - 1$ is proven by lattice fringes, but is not underpinned by \mathbf{q}_F and does not constrain assumed homology.

Keywords: HRTEM, tetradymite group, chemical-structural modularity, minimal shift condition, polysomatism

INTRODUCTION

The recent overview of minerals in the system Bi-Te-Se-S (Bi_xX_y , $X = \text{Te, Se, S}$) shows the system to include 19 species and several unnamed phases (Cook et al. 2007a). Phases in this system have rhombohedral- or trigonal-layered structures; exceptions include orthorhombic ($Pbnm$) bismuthinite (Bi_2S_3) and guanajuatite (Bi_2Se_3). In the layered structures, the “ c ” lattice parameter varies with composition in a non-linear way but the “ a ” parameter is constant at $\sim 4 \text{ \AA}$. Lind and Lidin (2003) used 4-dimensional superspace formalism (4D) to derive a general model in which all structures are included within the 4D group $P: R\bar{3}:m\bar{1}1$, with cell parameters $a \sim 4.2 \text{ \AA}$ and $c_{\text{sub}} \sim 5.7 \text{ \AA}$.

The non-systematic variation of the “ c ” parameter with composition is one of the characteristics of mixed-layer compounds. These belong to the broad family of modulated struc-

tures, since they are built by one or several “modules” that can differ in size (thickness), chemistry, and, in some cases, in the internal structure (e.g., Amelinckx et al. 1989). Such modules can be mixed in a periodic or quasi-periodic manner to generate superstructures.

In the tetradymite group, one of the modules is the X-Bi-X-Bi-X [5-atom-thick layer (mod5) of which the tetradymite structure, Bi_2X_3 is the “archetype”]. The other is considered a two-layer thick module (Bi-Bi) or Bi_2 , (mod2) (e.g., Imamov and Semiletov 1971). Using mod2 and mod5 for band structure calculations, Gaudin et al. (1995) proposed an oxidation state balance as $n(\text{Bi}^0)_2 \cdot m(\text{Bi}^{3+})_2(\text{X}^{2-})_3$, where metallic Bi-Bi bonds occur within the zero-valent Bi_2 layer and van der Waals gaps separate adjacent mod5-mod5 layers.

The general validity of the above “mod5 and mod2” model was questioned by Frangis et al. (1990) based on high-resolution transmission electron microscopy (HRTEM) studies of synthetic compounds of the type M_{2+6}X_3 , ($M = \text{Bi, Sb, Ge}$; $X = \text{Te, Se}$);

* E-mail: Cristiana.Ciobanu@adelaide.edu.au

$0 \leq \delta \leq 0.4$. Considering the building modules to be formed by addition of M-X (instead of M-M layers) to the Bi_2X_3 archetype, then such modules can indeed account for the structures studied by Frangis et al. (1990). The series can be expanded toward $\delta \rightarrow 1$, where the limiting phase ($\delta = 1$) is considered a hypothetical BiTe_{ccp} (NaCl-type cubic closed packed structure).

In this study, we formalize a model with application to the entire tetradymite group by corroborating previous studies and expanding existing models to the Bi-rich part of the group that has not been studied previously. Additionally, the validity of this model is tested for samples in the compositional range Bi_2X_3 - Bi_8X_3 , using electron diffraction and HRTEM imaging. The nanoscale characterization relative to variation in the Bi/X ratio for the analyzed samples is then used for genetic considerations.

CRYSTAL-STRUCTURAL CONSIDERATIONS

Two homologous series can be derived from the Bi_2X_3 archetype (X-M-X-M-X) by using an accretional principle to obtain building modules with incremental width. Both series include structures built by a single type of module, as well as structures formed by various combinations of the two module types. Such “accretional” and “combinatorial” structural-building principles form the foundation for homologous series of sulfosalts (e.g., Makovicky 1997). The two series are (1) chalcogen-rich series: $\text{M}_{p+\varepsilon}\text{X}_{p+1}$ ($p \geq 2$, integer; $\varepsilon < 1$), modules representing layers with symmetric M vs. X configuration (X-M-X-M-X-M-X...)

obtained by addition of $n(\text{M-X})$ layers, and (2) metal-rich series: $\text{M}_{2(k+\delta)}\text{X}_3$ ($k \geq 1$, integer; $\delta < 2$), modules resulting from layers with non-symmetric M vs. X arrangement (X-M-X-M-X-M-M...) obtained by addition of $n(\text{M-M})$ layers.

The resulting building modules for both series are characterized by the same incremental width and odd number of single layers, i.e., $N = 2p + 1$ ($p \geq 2$) and $N = 2k + 3$ ($k \geq 1$), respectively, but with different compositions, e.g., the symmetric modules M_3X_4 (mod7), M_4X_5 (mod9), and M_5X_6 (mod11) in the first series correspond to the non-symmetric modules M_4X_3 (mod7'), M_6X_3 (mod9'), and M_8X_3 (mod11') in the second series. In the metal-rich series, the building modules are zero-valent if the oxidation state of the metal is M^{3+} ($\text{M} = \text{Bi}, \text{Sb}$), but this can be achieved in the chalcogen-rich series only if a combination of M^{3+} ($\text{M} = \text{Bi}, \text{Sb}$) and M^{2+} ($\text{M} = \text{Ge}, \text{Pb}$) is considered.

Those phases with δ or $\varepsilon = 0$ are built by a single type of module consisting of N layers, whereas phases with δ or $\varepsilon \neq 0$ are built by intergrowths of two module types with consecutive k or p numbers (modules with incremental width). Values of k and p can be estimated by considering the structural formulae given above for each series and the types and the modules in the stacking sequence can be calculated using the formulae given in Table 1.

A consequence of homology in the tetradymite group is that the structural modules are able to adjust to incremental chemical changes across the compositional range. This fits with the Bi-

TABLE 1. Calculated γ_{fr} , γ , and c values for the two series shown in Figure 1b

M_xX_y ; x, y = smallest integers M = Bi (Sb, Ge, Pb) X = Te, Se, S	at% X	$\text{Bi}_{2k+\delta}\text{X}_3$ k ≥ 1 ; $\delta < 2$	k	Metal-rich series: Tetradymite group			γ_{fr}	γ	c (Å)
				$\delta = 0$	$0 < \delta \leq 1$	$1 < \delta < 2$			
				Structural modules in the sequence Bi_{2k}X_3 S'(Bi _{2k} X ₃).L'[Bi _{2(k+1)} X ₃]					
M_{14}X_3	17.7	Bi_{14}X_3	7	17'			0.0588	1.588	102
M_8X_3	27.3	* Bi_8X_3	4	11'			0.0909	1.636	66
M_7X_3^1	30.0	* Bi_7X_3	3		(1 × 9')(1 × 11')		0.1000	1.650	120
M_7X	33.3	* Bi_6X_3 (H)	3	9'			0.1111	1.667	18
M_{11}X_6	35.3	$\text{Bi}_{5.5}\text{X}_3$	2			(1 × 7')(3 × 9')	0.1176	1.676	204
M_4X_3	37.5	* Bi_2X_3	2		(1 × 7')(1 × 9')		0.1250	1.688	96
M_{14}X_9	39.1	* $\text{Bi}_{4.67}\text{X}_3$	2		(2 × 7')(1 × 9')		0.1304	1.696	138
$\text{M}_{23}\text{X}_{15}$	39.5	$\text{Bi}_{4.6}\text{X}_3$	2		(7 × 7')(3 × 9')		0.1316	1.697	456
M_3X_2	40.0	$\text{Bi}_{4.5}\text{X}_3$ (H)	2		(3 × 7')(1 × 9')		0.1333	1.700	60
$\text{M}_{22}\text{X}_{15}$	40.5	$\text{Bi}_{4.4}\text{X}_3$	2		(4 × 7')(1 × 9')		0.1350	1.703	222
$\text{M}_{17}\text{X}_{12}$	41.4	$\text{Bi}_{4.25}\text{X}_3$	2		(7 × 7')(1 × 9')		0.1379	1.707	348
M_4X_3^1	42.9	* Bi_4X_3	2	7'			0.1429	1.714	42
M_6X_5^1	45.5	$\text{Bi}_{3.6}\text{X}_3$ (H)	1			(1 × 5)(4 × 7')	0.1515	1.727	66
M_7X_6	46.1	$\text{Bi}_{3.5}\text{X}_3$	1			(1 × 5)(3 × 7')	0.1538	1.730	156
M_8X_7^1	46.7	$\text{Bi}_{3.42}\text{X}_3$ (H)	1			(2 × 5)(5 × 7')	0.1556	1.733	90
MX^1	50.0	* Bi_3X_3 (H)	1		(1 × 5)(1 × 7')		0.1667	1.750	24
M_8X_9	52.9	$\text{Bi}_{2.67}\text{X}_3$	1		(2 × 5)(1 × 7')		0.1765	1.765	102
M_5X_6	54.5	$\text{Bi}_{2.5}\text{X}_3$	1		(3 × 5)(1 × 7')		0.1818	1.773	132
M_4X_5^2	55.6	$\text{Bi}_{2.4}\text{X}_3$ (H)	1		(4 × 5)(1 × 7')		0.1852	1.777	54
$\text{M}_{13}\text{X}_{17}$	56.7	$\text{Bi}_{2.29}\text{X}_3$	1		(29 × 5)(5 × 7')		0.1889	1.783	360
M_3X_4^2	57.1	$\text{Bi}_{2.25}\text{X}_3$ (H)	1		(7 × 5)(1 × 7')		0.1905	1.786	84
M_7X_7	58.3	$\text{Bi}_{2.14}\text{X}_3$	1		(13 × 5)(1 × 7')		0.1944	1.792	144
$\text{M}_{19}\text{X}_{27}$	58.7	$\text{Bi}_{2.11}\text{X}_3$	1		(17 × 5)(1 × 7')		0.1957	1.793	552
M_7X_{10}	58.8	$\text{Bi}_{2.1}\text{X}_3$ (H)	1		(19 × 5)(1 × 7')		0.1961	1.794	204
M_9X_{13}	59.1	$\text{Bi}_{2.09}\text{X}_3$	1		(26 × 5)(1 × 7')		0.1971	1.796	822
$\text{M}_2\text{X}_3^{1,2}$	60.0	* Bi_2X_3	1	5			0.2000	1.800	30

Notes:

* = Phases analyzed in this study.

S', L' = non-symmetric modules (X-Bi-X-Bi-X-Bi...); bold: module type.

S' = (k + 1)(y/3) - x/2; L' = x/2 - k(y/3); x, y = calculated as multiple of 2 and 3, respectively.

N1 = S'(2k + 3) + L'(2k + 5).

$\gamma_{\text{fr}} = (S' + L')/N1$; $\gamma = 3[S'(k + 2) + L'(k + 3)]/N1$.

c = d₁N₁ = d₁(S' + L')/γ_{fr} (multiplied by 3 for R), d₁ = 2 Å.

H = phases P3m1; all others are R3m.

^{1,2} = Stoichiometries corresponding to known minerals in the tetradymite group and chalcogen-rich series, respectively (see Cook et al. 2007a, 2007b).

Te and Bi-Se phase diagrams (e.g., Okamoto and Tanner 1990; Okamoto 1994) showing that an infinite number of stacking sequences can account for continuous compositional variation in the 0 to 60 at% X range (Bi-Bi₂X₃).

Tetradymite group: the “mod5 and mod2” model

The metal-rich series above represents a homologous description of the tetradymite group, i.e., Bi_{2(k+δ)}X₃, where k is the homologue number. The building module that changes from one compound to another is derived from the tetradymite archetype, i.e., Bi_{2k}X₃, (k ≥ 1) for homologues with δ = 0. Intermediate phases (δ ≠ 0) can be written as intergrowths between two homologues built by modules with incremental width, i.e., S'(Bi_{2k}X₃)·L' [Bi_{2(k+1)}X₃], where S' and L' are the numbers of short and long modules, respectively, with non-symmetric M to X arrangement along the c axis.

In the model of Imamov and Semiletov (1971), the building units remain the same, i.e., “mod5” and “mod2.” The thicknesses of the Bi₂ and Bi₂X₃ modules are ~0.4 and ~1 nm, respectively. The authors suggested the term “compositional polytypism” to underline the structural principles and modules common to all phases despite their variable compositions. Shelimova et al. (2000) considered that the structural formula nBi₂·mBi₂X₃ could be used to describe homology in the series.

One-dimensional interface modulated superstructures

The series M_{2+δ}X₃ (δ < 1) studied by Frangis et al. (1990) can also be expressed by the structural formula given for the chalcogen-rich series. The compositional range of this series overlaps with that of phases from the tetradymite group, i.e., with k = 1 and δ < 1. Pairs of compounds from the two series with the same composition will, however, have different stacking sequences (Table 1) due to the chemical differences between the symmetric and non-symmetric modules. Phases from the chalcogen-rich series were found to be N-fold superstructures (N = number of single layers in the structure) of a c_{sub}/3 = d₁ ~ 0.2 nm. Considering this as an average interlayer spacing between two consecutive layers along the c axis, Frangis et al. (1990) used the fractional shift method of van Landuyt et al. (1970) to

define a structural modulation $\mathbf{q}_F = \gamma_F \mathbf{c}_{sub}^*$ [γ_F , \mathbf{c}_{sub}^* and \mathbf{q}_F are our notations and correspond to γ , \mathbf{H}_0 , and \mathbf{q} used by Frangis et al. (1990)]. The γ_F value is (1) $\gamma_F = 1/N$ for phases with $\varepsilon = 0$ [structures with a single type of module: M_pX_{p+1}; i.e., (2p + 1)-layers]; (2) $\gamma_F = (S + L)/N$ for phases with $\varepsilon \neq 0$ [intergrowths of two module types with consecutive p: S(M_pX_{p+1})·L(M_{p+1}X_{p+2}); S, L = numbers of short and long modules with symmetric M to X arrangement along c]. In real space, the magnitude of q_F is either c/3 or c (R or H symmetry) or a fraction (S + L) of this parameter for structures in categories 1 and 2, respectively (Table 1).

Some of the structures in category 2 give incommensurate or pseudo-incommensurate electron diffraction patterns (EDPs), i.e., either streaks with weak elongated maxima instead of sharp superstructure reflections (Fig. 3f in Frangis et al. 1990) or EDPs that can be indexed as commensurate but imply large repeat distances (e.g., Fig. 4b in Frangis et al. 1990); in the latter case q_F can be approximated by rational values rather than measured precisely.

Frangis et al. (1990) interpreted the physical meaning of the vector \mathbf{q}_F in terms of interface modulated structures based on the model of van Landuyt et al. (1970) to describe such structures. The basic cell, a hypothetical BiTe_{ccp} phase, consists of alternating Te and Bi layers along the c axis. If the cubic close packed cell is considered in a rhombohedral setting there are six sets of atoms with specific configurations in BiTe_{ccp} (Fig. 1a) Any of the stacking sequences in phases from either the M_{p+ε}X_{p+1} or Bi_{2(k+δ)}X₃ series can be derived from the basic BiTe_{ccp} structure by modifying the layer sequence (extraction or insertion of layers) at P = 2(p + 1) and Pγ = 2k + 3 periodicities, respectively, e.g., Figure 1a for the 11 and 11' modules. This can be obtained by closing or opening gaps (extraction or insertion of layers) along the P (P') interface planes and shifting the layers above these planes up or down so that the net of atoms is rearranged into a rhombohedral matrix. The array of atoms forming a unit cell will be always repeated after three units of a stacking sequence.

Considering that the structural modulation is driven by the displacements along the interface planes, phases built by modules with the same width (or combinations thereof) should give identical γ_F , irrespective of composition, i.e., whether built

TABLE 1.—EXTENDED

FN	M _{p+ε} X _{p+1} P ≥ 2; ε < 1	P	Chalcogen-rich series		γ _F	γ	c (Å)
			ε = 0	0 < ε < 1			
			Structural modules in the sequence				
			M _p X _{p+1}	S(M _p X _{p+1})·L(M _{p+1} X _{p+2})			
	M ₆ X ₉ (δ = 0.67)	8	17		0.0588	1.588	102
	M ₅ X ₆ (δ = 0.5)	5	11		0.0909	1.636	66
9H	M ₄ X ₅ (δ = 0.4)	4	9		0.1111	1.667	18
30H	M _{3,05} X ₄	3		(3x7)(1x9)	0.1333	1.700	60
21R	M ₃ X ₄ (δ = 0.25)	3	7		0.1429	1.714	42
12H	M _{2,14} X ₃	2		(1x5)(1x7)	0.1667	1.750	24
138R	M _{2,11} X ₃	2		(5x5)(3x7)	0.1739	1.761	276
51R	M _{2,1} X ₃	2		(2x5)(1x7)	0.1765	1.765	102
66R	M _{2,08} X ₃	2		(3x5)(1x7)	0.1818	1.773	132
15R	M ₂ X ₃	2	5		0.2000	1.800	30

FN = notation used by Frangis et al. (1990); italics = analyzed phases not explicitly noted.

S, L = symmetric modules (X-Bi-X-Bi-X-Bi-X...); bold: layer type.

S = y(p + 1) - x(p + 2); L = x(p + 1) - py; x, y = calculated as multiple of 2 and 3, respectively.

N2 = S(2p + 1) + L(2p + 3).

γ_F = (S + L)/N2; γ = 3[S(p + 1) + L(p + 2)]/N2.

c = d₁N2 = d₁(S + L)/γ_F (multiplied by 3 for R); d₁ = 2 Å.

by symmetric- or non-symmetric modules (Fig. 1b; Table 1). If this is true the two series are isoconfigurational (cf. Lima de Faria et al. 1990).

The general 4D model: One-dimensional sawtooth displacive modulation

Lind and Lidin (2003) investigated four structures from the Bi-Se system (Bi_2Se_3 , Bi_4Se_3 and Bi_8Se_9 , BiSe) by single-crystal X-ray diffraction and refinement of the data using two models that employed 4D formalism. Commensurate diffraction patterns were obtained for Bi_2Se_3 and Bi_4Se_3 , whereas Bi_8Se_9 and BiSe gave incommensurate diffraction patterns. A modulation vector was defined as $\mathbf{q} = \gamma\mathbf{c}^*$ (i.e., $\mathbf{c}_{\text{sub}}^*$). The reported γ range (1.80–1.70) is extrapolated from phases in the studied interval (Bi_2Se_3 – Bi_4Se_3) to the composition of Bi_3Se_2 phase; not including phases on the Bi-rich side of the system.

To interpret this modulation, Lind and Lidin (2003) employed two modeling options involving wave functions that have converged in the refinement of the structures. Of these, the two-atom model based on a displacive sawtooth modulation of the Se atom is more relevant for the physical meaning of vector \mathbf{q} . The sawtooth pattern formed by the homoatomic intervals (of Se and Bi) along the four-dimensional axis (x_4) will remain the same for all structures, but the length of these intervals varies with composition from one compound to another (modulation \mathbf{q}). We note that the model should also apply to the chalcogen-

rich series since the M_pX_{p+1} modules were derived in the same accretional manner as the $\text{Bi}_{2k}X_3$ modules. This would lead to similar changes in homoatomic periodicities for the two atoms occupying the same rhombohedral lattice.

The relative periodicities of the two atom types can be intuitively shown from projections of the structures onto (210) (Fig. 2). We observe that the homoatomic arrays (d_{4D}) across the stacking sequence are straight (Figs. 2a and 2b; left side) only for structures built by a single type of module; they otherwise form zigzag lines (Fig. 2c) named “incommensurate periodicities” (Lind and Lidin 2003). Conversion into a (3 + 1)-dimensional model is made by taking d_{4D} , the average interlayer interval along the x_4 axis [$d_{4D} = (1/3)c_{\text{sub}}$], equivalent to the interlayer distance along the 3-dimensional axis (x_3) along which the distance between adjacent layers is $d_{3D} = (1/3)c_{\text{sub}} = d_1$. For example, for the isoconfigurational modules 11' (Bi_8X_3) and 11 (M_4X_6), d_{4D} corresponds to a third of the c_{sub} axis or 6/18 (Figs. 2a and 2b; right side). The \mathbf{q} vector represents $(3d_{4D}/N)[001]^*$; translated into direct space this value is $1/\gamma = N/(3d_{4D})$. The γ value can be calculated by observing that $d_{4D(\text{Bi})} = k + 2$ and $d_{4D(X)} = p + 1$ for any $\text{Bi}_{2k}X_3$, M_pX_{p+1} modules, respectively, and substituting in the relation $\gamma = 3d_{4D}/N$ (formulae given in Table 1). Values were calculated up to $M_{14}X_3$ (γ to 1.588; Table 1). They show that γ decreases linearly with X at% (or Bi/X) and $\gamma \rightarrow 1.5$ for X at% $\rightarrow 0$ (Bi/X $\rightarrow \infty$) (Fig. 3).

Summary: Which model?

The two modulation vectors with application to structures from the tetradymite group have different meanings and have been defined using a conventional approach, a three-dimensional approach (3D; \mathbf{q}_F) as well as superspace formalism (4D; \mathbf{q}). The questions to be addressed are as follows: (1) is the linear trend between γ and composition obtained from calculated values confirmed by measurements? (2) Will the diffraction patterns confirm that the two types of modules, i.e., $\text{Bi}_{2k}X_3$ and M_pX_{p+1} (where $k = p - 1$) are isoconfigurational? (3) Does vector \mathbf{q}_F describe the same trend as \mathbf{q} ? (4) Can the results constrain which of the two structural formulae, $n\text{Bi}_2 \cdot m\text{Bi}_2X_3$ or $S'(\text{Bi}_{2k}X_3) \cdot L'[\text{Bi}_{2(k+1)}X_3]$, is underpinned by the \mathbf{q}_F vector and which of these provides a homologous description of the series?

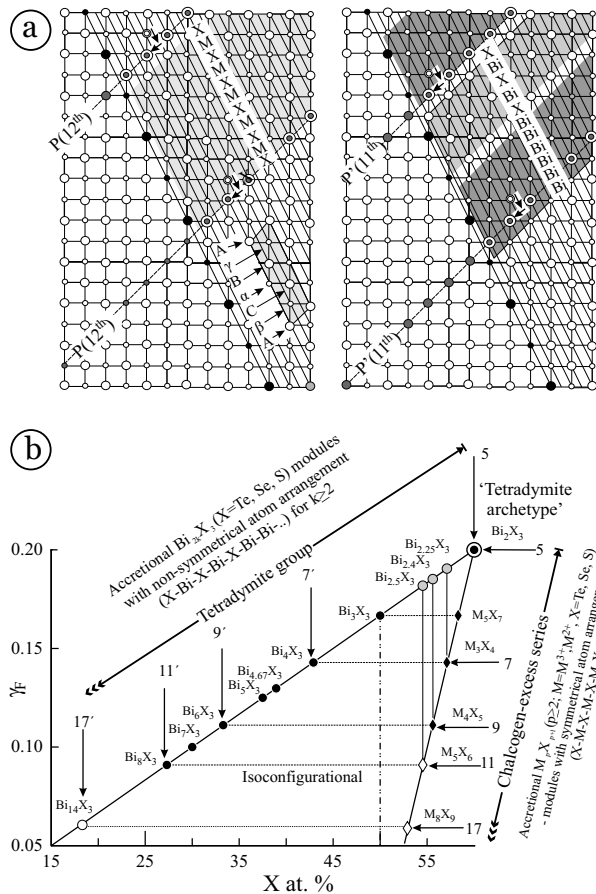


FIGURE 1. (a) Module derivation in the chalcogen-excess series (left) and the tetradymite group (right) from a cubic closed packed structure (e.g., BiTe_{cep}) by extracting layers at periodicity P and P', respectively. The layers above these displacement planes are successively shifted downward and laterally (short arrows) to close the gaps formed. The stacking mode is cubic but the separation of successive atom layers is modulated with an 11-layer period. The six atomic positions in the BiTe_{cep} structure are shown on the left side of the figure. Roman letters: Te; Greek letters: Bi. Large circles: chalcogen (X = Te, Se, S); small circles: metal/Bi. (b) Plot of γ_F vs. at% X for the two homologous series discussed in the text: (1) $\text{Bi}_{2k+\delta}X_3$ ($k \geq 1$; $\delta < 2$), tetradymite group (circles); (2) $M_{p+\varepsilon}X_{p+1}$ ($p \geq 2$; $\varepsilon < 1$) (rhombs). X = chalcogen; M = metal (M^{3+} , M^{2+}); empty symbols are hypothetical phases. Vertical lines show phases in the two series that have the same composition; note that compounds with more complex sequences in the tetradymite group (gray circles; Table 1), which correspond to single module types in the chalcogen-rich series have been obtained experimentally.

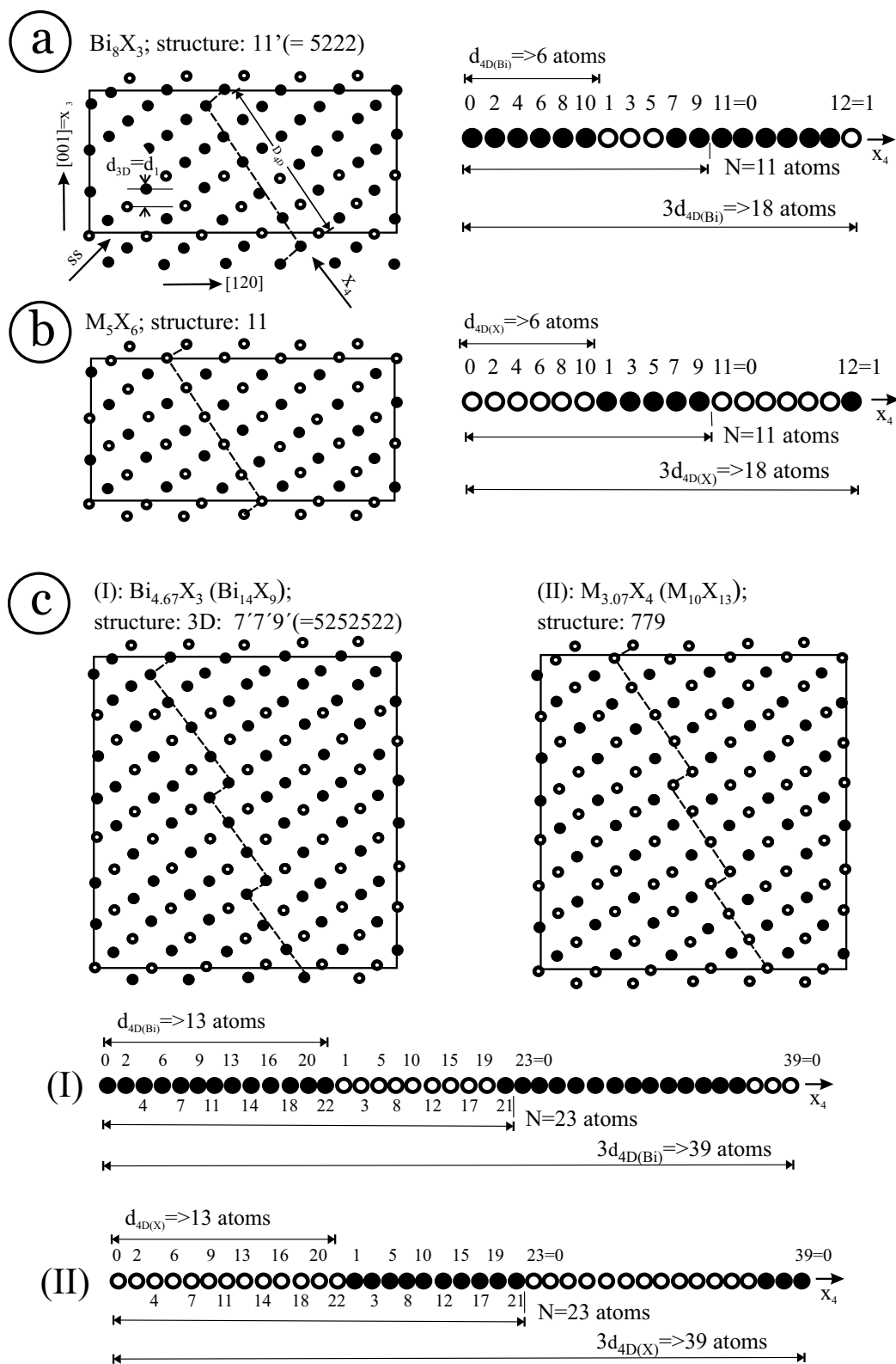


FIGURE 2. Projection of structures from the two homologous series onto (210) and corresponding homoatomic sequences (atomic positions numbered) along the four-dimensional axis (x_4). The dashed line shows the longer homoatomic interval (d_{4D}) across the stacking sequence corresponding to the interlayer distance along the c axis (subcell in 3-dimensional model ($d_{3D} = d_1$; see text). This line is straight for structures built by single types of modules (a, b) and zigzag in shape for those built by two types of modules (c). Black circles: Bi or metal; white circles: chalcogen. N = number of single layers in the stacking sequence (ss); this can be seen along the ss arrow.

SAMPLES AND EXPERIMENTAL DETAILS

Five samples from three localities were selected for study: (1) tellurobismuthite, found as millimeter-size nests in quartz within Cu-Au veins at Moberg, Norway (sample **M1**; Natural History Museum, University of Oslo); (2) pilsenite (sample **U1**); and (3) phase $\text{Bi}_{17}\text{Te}_{12}$ (sample **U2**), occurring as coarse, 3–4 mm, hexagonal platelets embedded in clay minerals and collected from an area with hydrothermal alteration in basaltic lava from Ilkivtsy (Transcarpathians, Ukraine). Samples 4 and 5 are bismuth tellurides found in association with native bismuth and gold in typical ore from the Au skarn at the Good Hope Mine, Hedley (B.C., Canada). In sample **H1**, joséite-B, with inclusions of hedleyite was studied from a centimeter-size patch within garnet-pyroxene skarn (Fig. 4b). Two millimeter-sized Bi-mineral patches in hedenbergite skarn (polished block H2) were labeled: **H2a**, comprises hedleyite and Bi_8Te_3 (Fig. 4c); sub-sample **H2b** consists of Bi_2Te (Fig. 4d); joséite-B envelops both patches.

Sample material was separated under the binocular microscope, mounted, and prepared as polished blocks. In all cases, except the two Hedley samples (**H1**, **H2a/b**), the sample material consisted of grains that are apparently monomineralic on the micrometer-scale. The homogeneity of these grains was checked by scanning electron microscopy (SEM). Compositions were determined by electron probe microanalysis (EPMA) using a Cameca SX-51 instrument, Adelaide Microscopy Centre, oper-

ating at an accelerating voltage of 20 kV and a beam current of 20 nA. Standards used were Bi_2Se_3 (Bi, Se), PbS (Pb, S), Ag_2Te (Te), and Sb_2S_3 (Sb).

For HRTEM examination, both crushed and microtome cut-and-thinned grains were mounted on carbon grids. Both types were prepared from all samples except **M1** from which mounts were only prepared from the crushed grains. Preparation of sample **H2a/b** was undertaken on patches extracted from a thin slice cut from the polished block H2 after it was subject to SEM/EPMA study. The instruments used for this study were a Philips 200CM transmission electron microscope, Adelaide Microscopy Centre, Australia, and the JEM 3010 transmission electron microscope at the Chemistry Department, Cambridge, U.K. The dual-beam focused ion beam (FIB) thinner at the Nova 200 Nanolab, University of New South Wales, Sydney, was also employed to extract slices from two polished blocks for HRTEM investigation. Slices were cut from **U2** (Fig. 4a) and across the hedleyite inclusions in **H1** (Fig. 4b).

Computer simulations based on the multislice method were performed for three phases (Bi_2Te_3 , BiTe , and Bi_2Te) using WinHREM 2.5 software. For the first two cases, the input data files used were ICSD 20289 (tellurobismuthite) and ICSD 100654 (tsumoite) from the Mineralogical Society of America Crystal Structure Database. In the third case, the parameters obtained for synthetic Sb_2Te (Agafonov et al. 1991) were introduced. The optical parameters used are spherical aberration coefficient: 1.3 mm; defocus spread: 83 Å; and beam convergence:

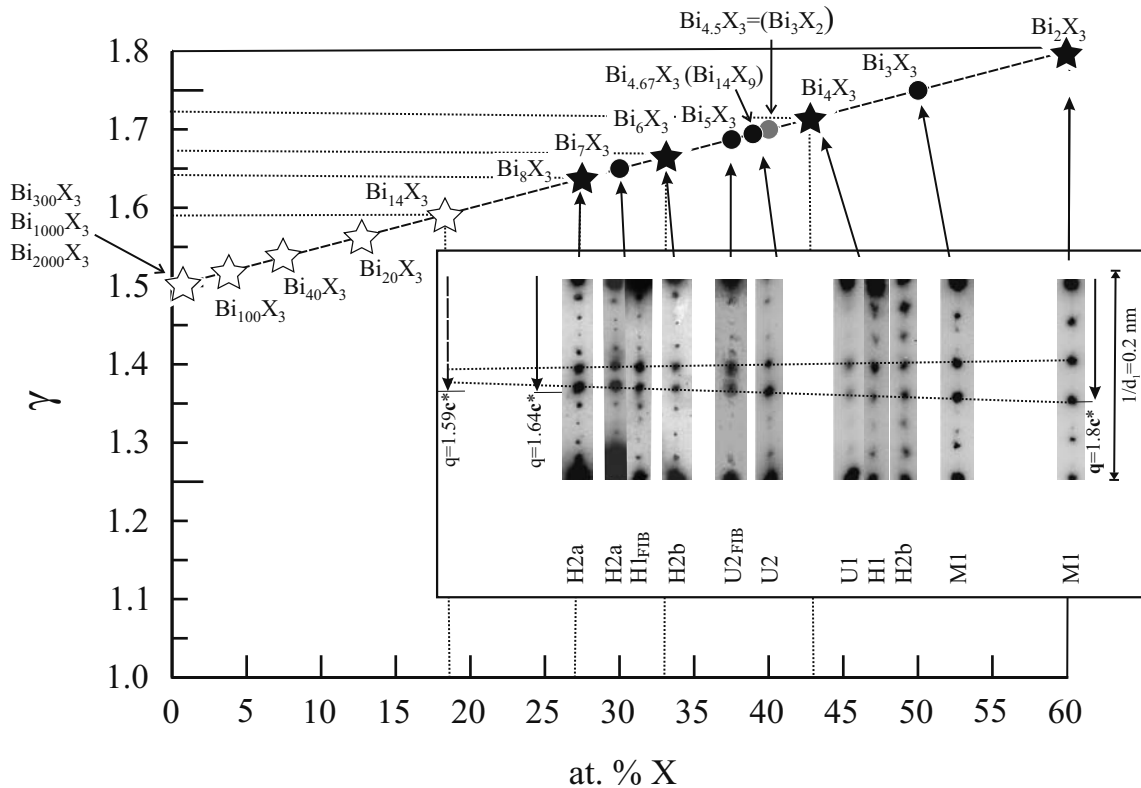


FIGURE 3. Linear correlation between calculated γ (Table 1) and composition for phases in the tetradymite group showing $\gamma \rightarrow 1.5$ for $X \rightarrow 0$. Stars and circles: phases with one and two module types, respectively. Empty symbols: hypothetical to very unlikely stable compounds; gray circle: the limit for extrapolated γ values of Lind and Lidin (2003). Inset: variation of q with composition as observed from electron diffraction patterns in this study. Dotted lines show the monotonical decrease of the interval between the two central reflections down to Bi_{14}X_3 .

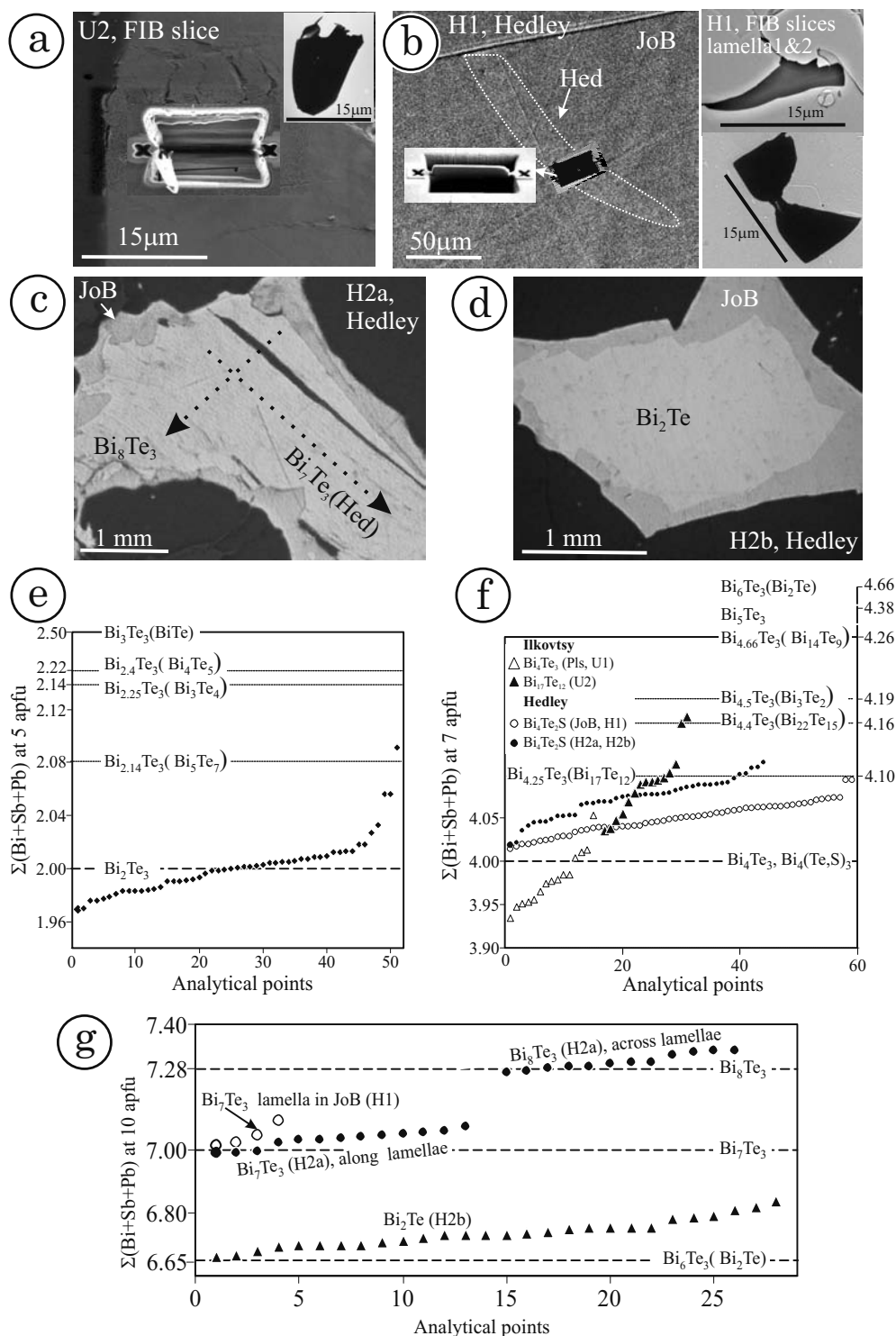


FIGURE 4. Back-scattered electron images showing analyzed samples. (a) Focused ion beam (FIB) slice (inset, dimensions of cut: 15/10/5 μm, thinned to a thickness ~100 nm) cut and extracted from sample U1 containing mounted material of composition Bi₁₇Te₁₂ (as measured by EPMA). (b) Location and detail of one of the two FIB cuts (inset) across an inclusion of hedleyite (Hed) within joséite-B (JoB); on the right-hand side, the two grid-mounted FIB slices; note the irregular shape due to the softness of this type of material. (c and d) Associations of Bi-rich phases in the two patches from H2 sampled for HRTEM investigation. Dotted arrows on c represent orientation of microanalytical profiles. (e) EPMA data for tellurobismuthite (M1) arranged in order of increasing Σ(Bi + Sb + Pb) calculated to 5 atoms per formula unit (apfu). Note spread of values across ideal stoichiometry. (f) EPMA data for JoB, pilsenite and Bi₁₇Te₁₂ arranged in order of increasing Σ(Bi + Sb + Pb) calculated to 7 apfu. (g) EPMA data for Hed, Bi₈Te₃, and Bi₂Te arranged in order of increasing Σ(Bi + Sb + Pb) calculated to 10 apfu. Dashed lines used as compositional grating for EPMA ranges; for comparison formulae are also normalized to X = 3 and as Bi_xX_y (x, y, smallest integers; brackets).

0.05 Å⁻¹. The simulations were selected from series of images obtained at different defocus/thickness parameters.

COMPOSITIONAL DATA

The specimens have compositions representing six discrete Bi/Te ratios in the Bi₂Te₃-Bi₈Te₃ range (Table 2). Three of these are recognized minerals, tellurobismuthite (Bi₂Te₃), pilsenite (Bi₄Te₃), and hedleyite (Bi₇Te₃), and three correspond to unnamed species, i.e., Bi₁₇Te₁₂ (=Bi_{4.25}Te₃), Bi₂Te (=Bi₆Te₃), and Bi₈Te₃. The composition Bi₄X₃ is also represented by joséite-B (Bi₄Te₂S), an S-bearing mineral that is relatively common in ore deposits.

Calculating each analysis on the total number of atoms in the formula corresponding to each mineral, a spread from ideal atomic Bi values is seen which is mostly within the range of analytical error (±2–3% relative; Figs. 4e–4g). Three of the 52 points from **M1** shows a greater offset from ideal stoichiometry [up to 2.09 apfu for a 5-atom unit corresponding to Bi_{2.14}Te₃ (=Bi₅Te₇)].

The unnamed phases are plotted on the same diagrams. The inner part of sample **H2a** (Fig. 4c) gives different compositions depending on whether the measurements are performed along (Bi₇Te₃), or across the lamellae (Bi₈Te₃). The compositional variation in all samples relates to nano-scale inhomogeneity as will be shown in the following sections.

ELECTRON DIFFRACTION PATTERNS AND HIGH-RESOLUTION IMAGES

Measurements and calculations for characteristic values have been obtained from the $[\bar{1}10]_R \equiv [110]_h$ zone axis on electron diffraction patterns (EDPs; Fig. 5) that are representative for all the phases in the analytical range, i.e., Bi₂X₃-Bi₈X₃, (X = Te, S). Three-integer indexation, corresponding to the subscript R, is with respect to a rhombohedral subcell and (3 + 1) integer (*hklm*) indexation, whereas subscript h is with respect to the hexagonal cell setting as given above. The EDPs show first the distance

TABLE 2. Electron probe microanalytical data for bismuth tellurides

Location	Moberg, Norway Orogenic Au				Transcarpathians, Ukraine Clay alteration in basalts				Hedley, B. C., Canada Auskarn					
Sample	M1		U2		U1		H1		H1, lamellae		H2a/b			
Mineral/phase	Tellurobismuthite		Pilsenite		Unnamed Bi ₁₇ Te ₁₂		Joseite-B		Hedleyite		Joseite-B			
wt%	Mean	S.D.	Mean	S.D.	Mean	S.D.	Mean	S.D.	Mean	S.D.	Mean	S.D.		
No. of points	51		14		15		59		4		44			
Pb	0.02	0.05	0.26	0.11	0.12	0.11	<mdl	<mdl	<mdl	<mdl	0.10	0.09		
Cd										0.23	0.13			
Bi	52.52	0.75	68.20	0.55	70.35	0.68	75.24	0.63	79.96	41.69	75.39	0.60		
Sb	0.33	0.05	0.21	0.05	0.20	0.05	0.21	0.06	0.38	0.09	0.16	0.04		
Te	47.06	0.68	31.49	0.53	29.44	0.50	21.29	0.25	20.49	14.81	22.05	0.21		
Se	0.93	0.06	0.11	0.04	0.42	0.07	0.04	0.03	0.01	0.19	0.09	0.06		
S	0.02	0.02	0.07	0.02	0.17	0.02	3.09	0.06	0.04	1.50	2.78	0.07		
Total	100.88		100.34		100.71		99.88		100.88		100.80			
Formulae	calc. to 5 apfu		calc. to 7 apfu		calc. to 29 apfu		calc. to 7 apfu		calc. to 10 apfu		calc. to 7 apfu			
Pb	0.001	0.002	0.02	0.007	0.03	0.03	0	–	0	–	0.005	0.005		
Bi	1.98	0.022	3.94	0.034	16.82	0.17	4.03	0.020	6.99	0.037	4.05	0.026		
Sb	0.02	0.003	0.02	0.005	0.08	0.02	0.02	0.006	0.06	0.013	0.01	0.004		
Sum M	2.00	0.022	3.98	0.032	16.94	0.16	4.05	0.018	7.04	0.036	4.07	0.022		
Te	2.90	0.022	2.98	0.036	11.53	0.15	1.87	0.022	2.93	0.032	1.94	0.018		
Se	0.09	0.006	0.02	0.006	0.27	0.05	0.01	0.004	0.00	0.004	0.01	0.009		
S	0.00	0.004	0.03	0.009	0.27	0.03	1.08	0.020	0.02	0.020	0.97	0.021		
Sum (Te + S + Se)	3.00	0.022	3.02	0.033	12.07	0.16	2.95	0.018	2.96	0.036	2.93	0.022		
Location	Hedley, B. C., Canada Auskarn													
Sample	H2b		H2a		H2a		H2a	H2 (3 other grains)		H2 (6 other grains)				
Mineral/phase	Unnamed Bi ₅ Te ₇		Hedleyite (along)		Bi ₈ Te ₃ (across)		patch	Hedleyite		Bi ₈ Te ₃				
wt%	Mean	S.D.	Mean	S.D.	Mean	S.D.	Mean all	Mean	S.D.	Mean	S.D.			
No. of points	28		12		12		24	30		55				
Pb	0.19	0.10	0.04	0.06	0.10	0.08	0.07	0.04	0.06	0.03	0.06			
Cd	0.23	0.14	0.26	0.16	0.28	0.12	0.27	0.21	0.10	0.23	0.13			
Bi	77.12	0.46	80.02	0.60	81.85	0.47	80.94	79.81	0.55	81.40	0.42			
Sb	0.28	0.05	0.20	0.06	0.18	0.06	0.19	0.22	0.05	0.17	0.05			
Te	22.76	0.41	20.54	0.22	18.59	0.21	19.56	20.42	0.23	18.84	0.29			
Se	0.09	0.03	0.07	0.04	0.09	0.03	0.08	0.08	0.04	0.07	0.03			
S	0.03	0.02	0.01	0.02	0.01	0.01	0.01	0.01	0.01	0.01	0.01			
Total	100.68		101.14		101.09		101.12	100.80		100.74				
Formulae	calc. to 3 apfu		calc. to 10 apfu		calc. to 11 apfu			calc. to 10 apfu		calc. to 11 apfu				
Pb	0.005	0.003	0.004	0.005	0.01	0.008	0.01	0.00	0.01	0.00	0.01			
Bi	2.00	0.014	7.00	0.030	7.97	0.034	7.48	7.00	0.03	7.93	0.04			
Sb	0.01	0.002	0.03	0.009	0.03	0.009	0.03	0.03	0.01	0.03	0.01			
Sum M	2.02	0.014	7.03	0.029	8.01	0.028	7.52	7.04	0.03	7.97	0.04			
Te	0.97	0.013	2.94	0.023	2.96	0.027	2.95	2.93	0.03	3.01	0.04			
Se	0.01	0.002	0.02	0.009	0.02	0.007	0.02	0.02	0.01	0.02	0.01			
S	0.005	0.004	0.01	0.009	0.00	0.007	0.01	0.01	0.01	0.01	0.01			
Sum (Te + S + Se)	0.98	0.014	2.97	0.029	2.99	0.028	2.98	2.96	0.03	3.03	0.04			

Note: Minor Cd contents not included in formula calculation.

between rows parallel to \mathbf{c}^* (d_a^*) varies little from one phase to another and consequently the “ a ” parameter, i.e., $a = (1/d_a^*)$ ($1/\cos 30^\circ$), is very similar across the compositional interval, i.e., $a = 0.434\text{--}0.441$ nm. Second, the distance (d_1^*) between main subcell reflections along rows parallel to \mathbf{c}^* has relative constant values ($1/d_1^* = d_1 = 0.19\text{--}0.2$ nm in real space). Finally the EDPs show the intensity of reflections varies across d_1^* and the brightest (first-order satellites) form a pair of reflections with equal intensity situated at the center of this interval.

Structures built by a single type of Bi_{2k}X_3 module

Electron diffraction patterns showing reflections situated at equal intervals within d_1^* where $d_N^* = (1/N)d_1^*$ (Figs. 5a–5d), were obtained for all phases with bulk compositions corresponding to Bi_{2k}X_3 ($\delta = 0$) for the interval $k = 1\text{--}4$. According to the structural formulae given in Table 1 these are representative of the building modules in this k range as follows: (1) $k = 1$, module 5: Bi_2Te_3 , tellurobismuthite (**M1**; Fig. 5a; note the similarity with the EDP obtained for synthetic Bi_2Te_3 by Frangis et al. 1990); (2) $k = 2$, module 7': Bi_4Te_3 , pilsenite (**U1**) and $\text{Bi}_4\text{Te}_2\text{S}$ [joséite-B, **H1**; **H2a** (Fig. 5b) and **H2b**]; (3) $k = 3$, module 9': Bi_6Te_3 [= Bi_2Te ; **H2b** (Fig. 5c), **U1** and **H1**]; and (4) $k = 4$, module 11': Bi_8Te_3 (**H2a**; Fig. 5d).

The number of reflections within the d_1^* interval increases by two for phases with consecutive k , i.e., 4, 6, 8, and 10 for $k = 1, 2, 3$, and 4, respectively (Figs. 5a–5d), indicating that they are $N = 2k + 3$ superstructures. This proves the accretional principle (homology in the group) considered for module formation, as well as the isoconfigurational relationships with the building modules from the chalcogen-excess series studied by Frangis et al. (1990). The variation in the intensity of superstructure reflections is discussed in the next sections.

Lattice images illustrating all the above structures (Fig. 6) show the incremental width by 0.4 nm for the suite of four modules with $k = 1$ to 4, i.e., modules 5, 7', 9', and 11' (Fig. 6a). It can also be seen that the modules can each be further subdivided into 5- and 2-units (Figs. 6b–6e) where the latter represents the double-Bi layer (Bi_2) with metallic bonds as discussed above. Such subdivisions are illustrated by the differences between images showing a simple, regular sequence of 5-modules (Tbs; lower part of Fig. 6b; note the change in the image due to variation of thickness at the top of the same grain; computer simulation in the insets) and those containing 1-, 2-, or 3- Bi_2 units (as separate rows; Figs. 6c–6e) between strips of width corresponding to the 5-module, i.e., ~ 1 nm. The 5-modules appear as wider, brighter strips of the same width on all the images, whereas the increasing distance between them, corresponding to the incremental number of Bi_2 units, is also marked by the presence of 1, 2, and 3 less bright rows (Figs. 6c, 6d, and 6e, respectively). Considering this interpretation, erratic addition/absence of individual Bi_2 units in sequences that are otherwise ordered (e.g., Figs. 6d and 6e) was observed in all samples.

One of the difficulties encountered for specimens containing phases with more than one Bi_2 unit is to appreciate the number of Bi_2 units relative to the 5-module. This is illustrated by the range of images obtained for the “same” phase, i.e., representing the unnamed Bi_2Te (Bi_6Te_3); Figure 7. For example, Figures 7a and 7b illustrate the change in the width of brighter strips for the

same image obtained by increasing the defocus. The variation in the width of the brighter strips can be seen at the same time across an image and can be attributed to the uneven thickness of a single grain (Fig. 7c). These aspects are often encountered when preparing TEM grids from very soft materials such as those analyzed here, due to the fact that they tend to bend and twist during preparation. Such deformational effects are shown in Figure 7d by the shift in the position of the brighter strips (lower left corner of the image) or by the swell in the central part of the image. The latter shows in what way this affects the defocus, and as a result the number of rows seen between the same strips can vary, i.e., from two (top right corner) to one (middle of the image). The best illustration for the fact that the internal configuration of Bi_{2k}X_3 structural modules consists of distinct, smaller, 5- and 2-units, as shown here and predicted from theoretical considerations (see above), was obtained on a very thin specimen (Fig. 7e, computer simulation in the inset). The sequence interpretation 9' (=522) is confirmed by the fast Fourier transform (Fig. 7f).

Structures built by intergrowths of Bi_{2k}X_3 modules

Electron diffraction patterns that show distribution of satellite reflections at variable spacing within the d_1^* interval (Figs. 5e–5h) were obtained from (1) sample **M1**, consisting of tellurobismuthite with small metal excess (Fig. 5e), and (2) samples with bulk compositions where $\delta \neq 0$, i.e., $k = 3$; $\delta = 1$: hedleyite (Bi_7Te_3 ; **H1**_{FIB slice} and **H2a**; Fig. 5h) and $k = 2$; $\delta = 0.25$: unnamed $\text{Bi}_{4.25}\text{Te}_3$ (= $\text{Bi}_{17}\text{Te}_{12}$; **U2**). The stacking sequences estimated from EDPs obtained from samples investigated by HRTEM (see following sections) give compositions **U2**: $k = 2$; $\delta = 0.67$: $\text{Bi}_{4.67}\text{Te}_3$ (= $\text{Bi}_{14}\text{Te}_9$; Fig. 5f) and **U2**_{FIB}: $k = 2$; $\delta = 1$: Bi_5Te_3 (Fig. 5g), which do not correspond to the measured EPMA composition for sample **U2** (see final section).

In the first case, the lattice images (Figs. 8a and 8b) that correspond to the EDP in Figure 5e are used to identify the stacking sequence. This shows alternating modules of 1 and 1.4 nm widths (Fig. 8a). Marginal fringes display an alternation of single and double bright rows placed at intervals of 1 nm width (Fig. 8b; computer simulation in the inset). The above aspects are interpreted as a regular 7'5 (=525) sequence corresponding to tsumoite (Bi_3Te_3 , Table 1); occasional stacking disorder is also observed (Fig. 8b, white rectangle inset).

Lattice images characteristic for hedleyite (Fig. 8c) show alternating fringes of 1.8 and 2.2 nm widths and correspond to the sequence 9'11' considered for this mineral (Table 1). The associated EDP for this mineral is shown in Figure 5h. The sequence that can be calculated for unnamed $\text{Bi}_{4.25}\text{Te}_3$, i.e., 7'7'7'7'7'7'9 (Table 1), has not been observed in TEM samples prepared from this material; lattice images corresponding to EDP in Figure 5f will be discussed in the next sections.

CHEMICAL-STRUCTURAL MODULARITY IN THE TETRADYMITE GROUP

Wave-modulation vector and compositional variation

The wave-like variation in the intensity of satellite reflections across the d_1^* interval (Fig. 5) indicates that a primary wave-modulation vector can be considered as $\mathbf{q} = \gamma[111]^*_R \equiv \gamma[003]^*_h$.

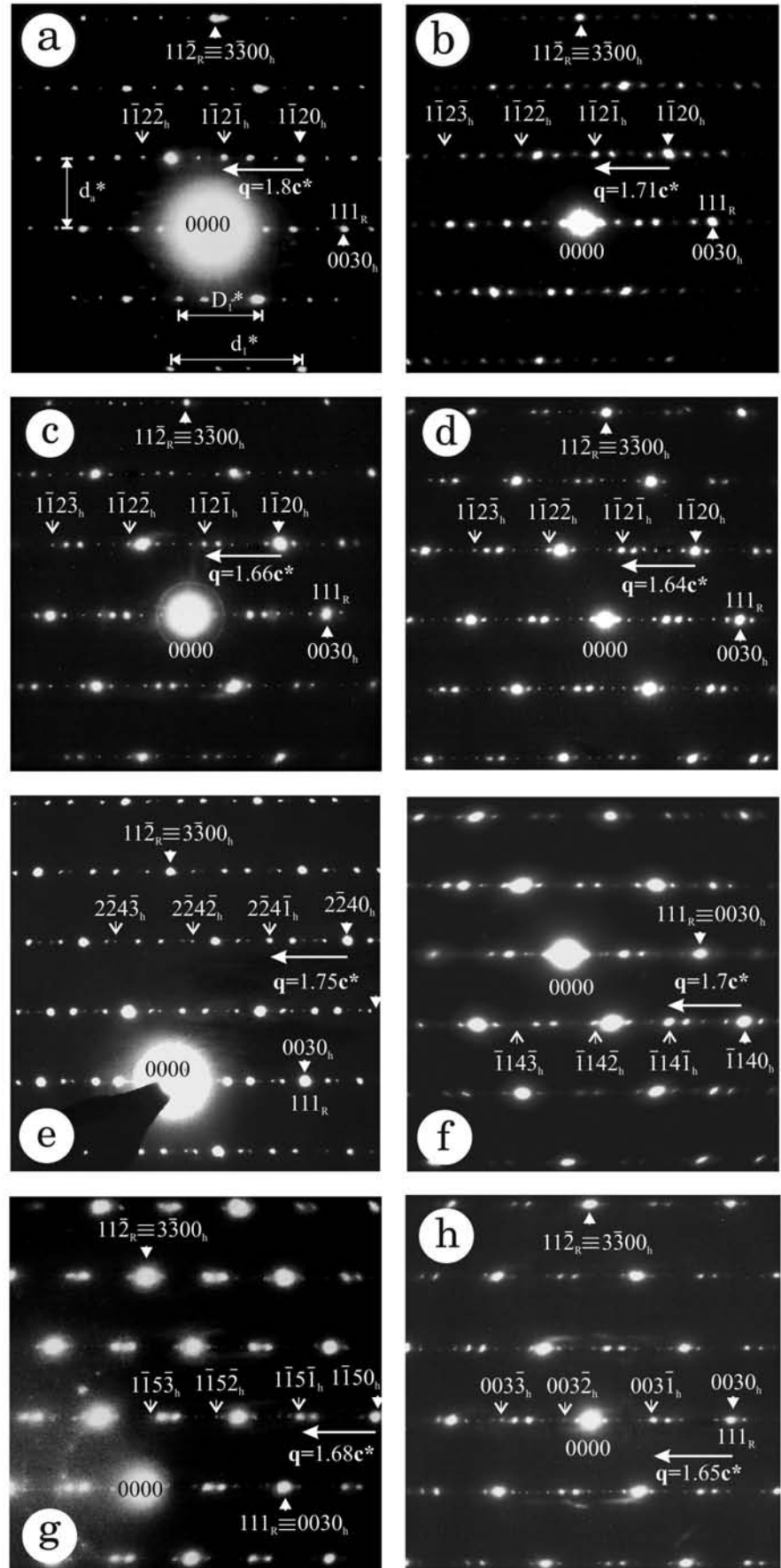


FIGURE 5. $[\bar{1}10]_R \equiv [110]_h$ zone axis on electron diffraction patterns (EDPs) that are representative for all the phases in the analytical range, i.e., $Bi_2X_3 - Bi_8X_3$, ($X = Te, S$). Three-integer indexing, corresponding to the subscript **R**, is with respect to rhombohedral subcell and $(3 + 1)$ integer $(hklm)$ indexing, whereas subscript **h** is with respect to the hexagonal cell setting (4D group $P: R\bar{3}:m\bar{1}1$; Lind and Lidin 2003). The arrows indicate positions of q prime as given in text. (a) Tellurobismuthite (M1). (b) Joséite-B (H1). (c) Unnamed Bi_2Te (H2b). (d) Unnamed Bi_8X_3 (H2a). (e) Phase with measured γ value corresponding to $Bi/X = 1$ interpreted as BiX (sequence 57'); $X =$ chalcogen (M1). (f) Phase with measured γ value (1.7) indicating $Bi/X \sim Bi_3X_2$ but for which the composition $Bi_{1.4}X_9$ (calculated $\gamma = 1.696$; Table 1) is considered based on the stacking sequence (sequence 7'7'9'; see text) (TEM sample U2). (g) phase with γ corresponding to $Bi/X = 5/3$; unnamed Bi_5X_3 (sequence 7'9') (U2_{FB}). (h) Hedleyite (H2a).

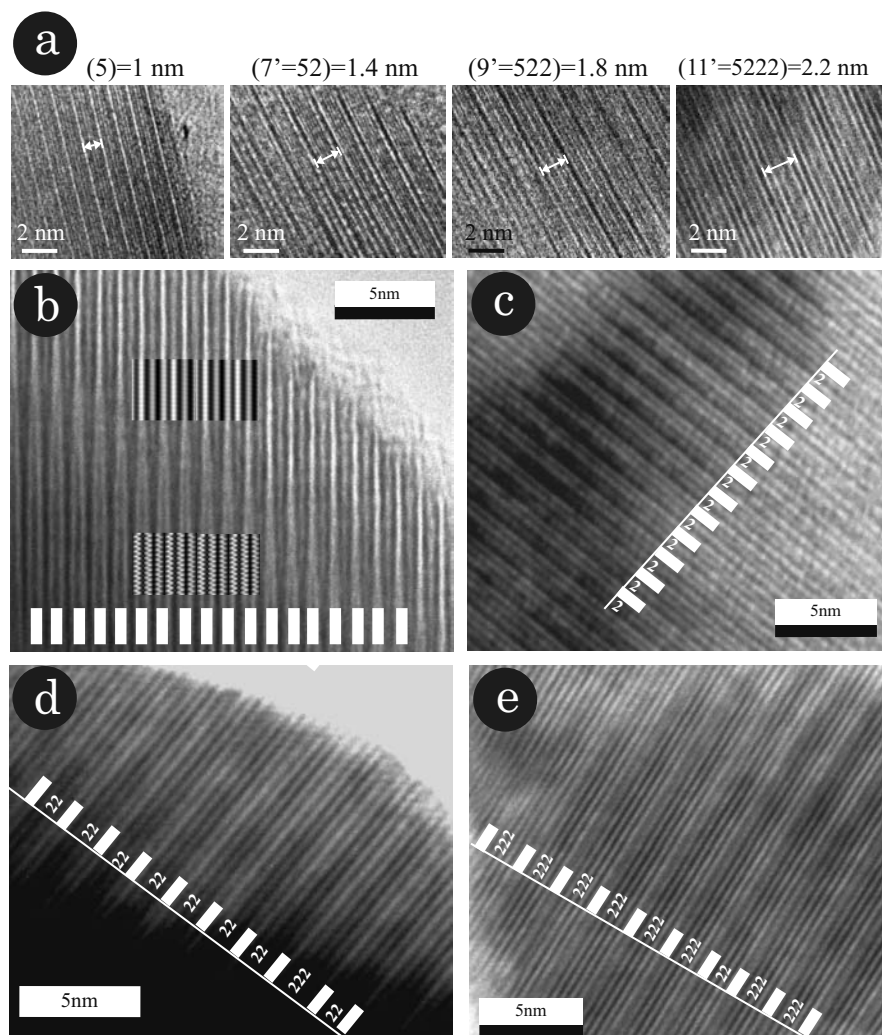


FIGURE 6. HRTEM images representative for stacking sequences in structures built by a single type of module (corresponding EDPs and samples are given in Figs. 5a–5d). (a) Incremental width for Bi_{2k}X_3 modules in the range $k = 1–4$; $X = \text{chalcogen}$ (b to e) lattice images showing that the Bi_{2k}X_3 modules with incremental width (from $k = 1$ to 4) appear subdivided into “mod2” and “mod5”-layer units according to the formula: $n\text{Bi}_2 \cdot m\text{Bi}_2\text{X}_3$, where $n/m = k - 1$; the 5 units are marked by white rectangles. Insets in b: Computer simulations for Bi_2Te_3 , showing the changes in the image due to differences in defocus, i.e., thickness/defocus at: 10/600 and 10/3600 for the lower and upper insets, respectively.

The weaker reflections correspond to high-order harmonics of \mathbf{q} (indexation of satellite reflections on EDPs in Fig. 5). As shown by Lind and Lidin (2003), \mathbf{q} corresponds to the distance (D_1^*) between any of the main subcell reflections on the EDPs, as the origin, and the furthest away of the two satellite reflections in the middle of the d_1 interval (the position referred to as \mathbf{q} prime). The distance between the pair of first-order satellites decreases from Bi_2X_3 to Bi_8X_3 and accordingly the \mathbf{q} vector decreases linearly with the increase in Bi content (or increase in the Bi/X ratio) (Fig. 4, inset). Values obtained for $\gamma = 3D_1^*/d_1^*$ by measurements on EDPs correspond within measurement error to the values given in Table 1, i.e., 1.8–1.64. The magnitude of \mathbf{q} in real space ($1/D_1 = D_1^*$) increases from 0.33 to 0.35 nm and gives c_{sub} values [$c_{\text{sub}} = (1/D_1)\gamma$] in the range 0.6 to 0.57 nm for Bi_2Te_3 to Bi_8Te_3 .

The present results confirm that the trend between γ and composition obtained for phases at the Bi-rich side of the system (Fig. 4, inset) remains linear and preserves the same slope as obtained by Lind and Lidin (2003). The γ values estimated from EDPs allow, however, only a rough identification of phases (especially for Bi-richer compositions); this can be obtained instead by estimation of stacking sequences as shown below.

Displacement vector and stacking sequences

Considering that all the investigated structures have the same rhombohedral subcell ($d_1 \sim 0.2$ nm) as those from the chalcogen-excess series, the displacement vector \mathbf{q}_F that links the structural modules to the chemistry according to the equation:

$$\mathbf{q}_F = (i/N)d_1^* = id_N^* \quad (1)$$

where $i = S' + L'$ (number of modules in the sequence), can be also used to estimate the stacking sequences for phases in the tetradymite group. The phases built by a single type of Bi_{2k}X_3 module (Fig. 9) have $i = 1$ and $\mathbf{q}_F = (1/N)d_1^*$, and thus the stacking sequences are easy to estimate directly from the number of superstructure reflections, as discussed above. It should be noted that if the formula $n\text{Bi}_2 \cdot m\text{Bi}_2\text{X}_3$ (e.g., Imamov et al. 1971) would be considered for the structural modules instead of Bi_{2k}X_3 , the value of “ i ” would differ from one phase to another ($i \neq 1$ for structures with $\text{Bi}_2 \neq 0$), contradicting the present observations.

Equation 1 is particularly useful for phases built by intergrowths of two modules with consecutive values of k , i.e., $S'(\text{Bi}_{2k}\text{X}_3) \cdot L'[\text{Bi}_{2(k+1)}\text{X}_3]$ (Figs. 10a–10d). In this case, the shortest interval observed between reflections can be used as a measure

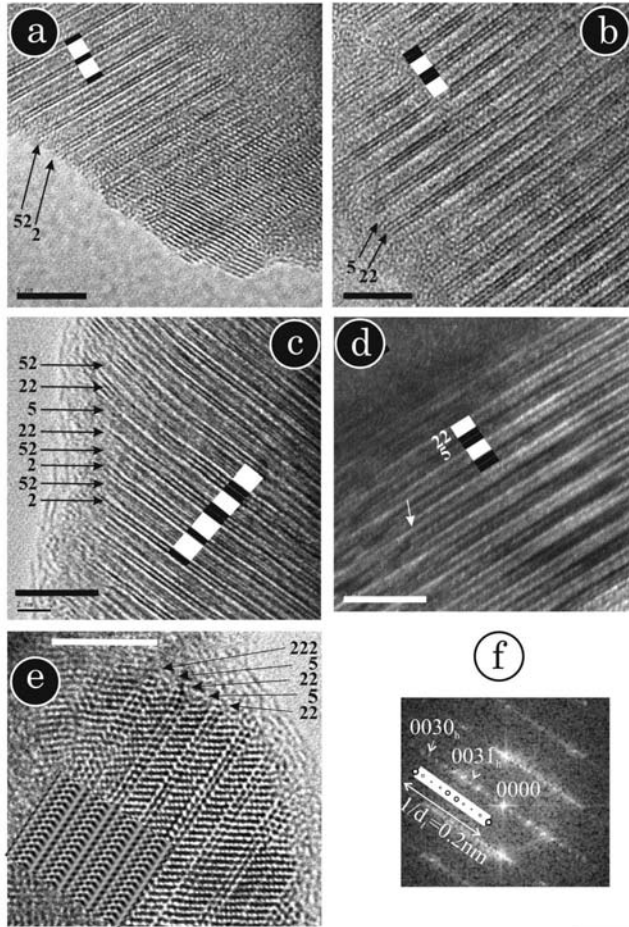


FIGURE 7. (a–e) HRTEM images showing the variability in the appearance of “522” sequences (module 9′) for the unnamed Bi_2Te phase as marked on the figures (a, b and e from sample **H1**; c and d from sample **U1**). The detail on image in e, obtained from a thin edge, clearly shows the different widths corresponding to the two types of units (mod2 and mod5). Computer simulation (inset) is shown for thickness/defocus at 2/300. Scale bars: 5 nm. (f) Fast Fourier transform confirming this phase as Bi_2Te (ninefold superstructure). Indexation for the hexagonal setting as in Figure 5.

(d_N^*) that gives the number of N intervals along d_1^* ; e.g., 12-, 16-, 20-, and 23-intervals for structures in Figures 10e–10h, respectively. Knowing that $q_F = id_N^*$ and the distance between the pair of brightest reflections in the middle of d_1^* is equal to the magnitude of q_F , the value of “ i ” can be easily found from the number of d_N^* intervals within this distance, e.g., $i = 2$ in three of the investigated structures and $i = 3$ in the fourth case (Figs. 10e–10h).

The module types in each structure can be graphically estimated from the distance between the two first-order satellites in the center of d_1^* , i.e., this distance ($q_F = id_N^*$) is shorter than the L' module and longer than the S' module. For example, the structure in Figure 10e has $d_5 < 2d_{12} < d_7$, and the fit for the observed “ $i = 2$ ” relative to N is $5 + 7' = 12$. This is in agreement with the $\text{Bi}/\text{X} = 1$ ratio corresponding to the measured $\gamma = 1.75$ (Fig. 3, inset). It should be noted, however, that such parameters obtained from the EDP are not discriminative between sequences

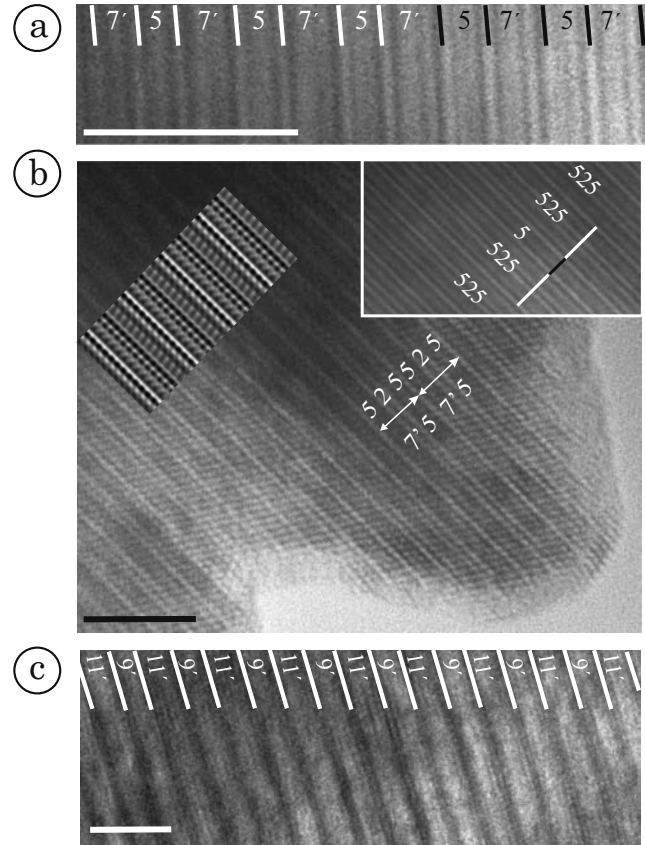


FIGURE 8. HRTEM images showing stacking sequences (interpretation as marked) in the BiX phase (EDP in Figure 5e; sample **M1**) (a, b) and (c) hedleyite (EDP in Figure 5h; sample **H2a**). Computer simulation (inset in b) for thickness/defocus conditions at 10/300. Scale bars: 5 nm.

of $57'$ and 57 that correspond to different compositions (BiTe and Bi_5Te_7 , respectively; see Table 1 for γ). In this case (Fig. 10e), the choice for the $7'$ module is based on the interpretation of lattice images (Fig. 8b).

In cases where the number k is known from the chemical formula and N is calculated as given above, values for S' and L' can be calculated from the relationship: $N = S'(2k + 3) + L'[2(k + 1) + 3]$ in which we substitute $S' = i - L'$. After substitution we obtain: $L' = N/2 - (2k + 3)i/2$ and $S' = (2k + 5)i/2 - N/2$. This gives the stacking sequences as: $(7' + 9') = 16$, $(9' + 11') = 20$, and $(7' + 7' + 9') = 23$, respectively, for the other three structures in Figures 10f–10h.

The significance of q_F as a displacement vector becomes apparent when this is considered as a component of the reciprocal lattice vector ($g_{t,m}$) describing the superstructure reflections for an interface modulated structure (DS) relative to a basic structure (BS) (Van Landuyt et al. 1970):

$$\mathbf{g}_{(m,t)} = \mathbf{H}_t + (1/d_N)(m - \mathbf{H}_t \cdot \mathbf{R})\mathbf{e}_u \quad (2)$$

where \mathbf{H}_t = position vector for reflections in BS, $1/d_N$ = distance between superstructure reflections (DS), m = index representing the order of DS reflections relative to a given t , \mathbf{R} = displacement vector along \mathbf{e}_u characterizing the structural shift in real space,

and \mathbf{e}_u = unitary vector perpendicular to the interface.

Considering that $\mathbf{q}_F = \gamma_F \mathbf{c}_{\text{sub}}^*$ and $\mathbf{c}_{\text{sub}}^* = d_1^* \mathbf{e}_u$, we can write $\mathbf{q}_F = (i/N)(1/d_1) \mathbf{e}_u = i(1/d_N) \mathbf{e}_u$. Rewriting $(1/d_N) \mathbf{e}_u = (1/i) \mathbf{q}_F$ and substituting into Equation 2, we obtain:

$$\mathbf{g}_{(m,t)} = \mathbf{H}_t + (1/i)(m - \mathbf{H}_t \cdot \mathbf{R}) \mathbf{q}_F \quad (3)$$

This relation shows that the value of $\mathbf{g}_{(m,t)}$ is equal to $(\mathbf{H}_t + \mathbf{q}_F)$ for the set of conditions $t = 0$ and $m = i$, meaning that \mathbf{q}_F can be identified with a displacement vector along the \mathbf{c}^* axis.

Fractional shifts and Bi_{2k}X_3 structural units (homology in the group)

The term $(\mathbf{H}_t \cdot \mathbf{R})/d_N$ in Equation 2 is a measure for the fractional shift between BS and neighboring DS reflections at a given position “t.” This can be directly observed by superimposing the diffraction patterns for the two structures, e.g., Bi_2Te_3 and BiTe_{ccp} structures (Fig. 9e) as discussed by Frangis et al. (1990) (Table A1 in Appendix A¹). Introducing the observed shifts into Equation 2, we obtain the position displacements for any “m” reflection in DS surrounding a “t” reflection in BS.

Based on the homology in the group, modules with consecutive k can be derived from one another, e.g., the 7'- from 5, the 9'- from 7-, the 11' from 9'-modules. This is schematically represented (Figs. 9f–9h) by showing the overlap between reflections in an N- and $(N - 2)$ -fold superstructure where the latter is considered as BS. In the case of phases built by two modules with consecutive k, and where $i = 2$, either of the two modules, S' or L' , can be considered as BS. For the three phases with $i = 2$ studied here (Figs. 10e–10g), the S' modules are chosen as BS for simplicity. In cases where $i > 2$, however, the choice for BS is restricted to the dominant module in the stacking sequence, e.g., in 7'7'9', $i = 3$ and BS is 7' (Fig. 10h). The number of layers for BS is thus given by the general formulae $(N - 2)/i$ and $(N + 2)/i$, dependent on whether S' or L' , respectively, is the dominant module.

Considering the above, the fractional shift $(\mathbf{H}_t \cdot \mathbf{R})/d_N$ at position t can be written as $\Delta d/d_N^*$ where Δd is calculated as a difference of segments. For example, consider Figure 10e where $\Delta d = t[d_{(N-2)/i}^* - id_N^*]$. After substituting $d_{(N-2)/i}^* = (1/d_1)[i/(N - 2)]$ and $d_N^* = (1/d_1)(1/N)$ into this equation we obtain:

$$\Delta d/d_N^* = 2ti/(N - 2). \quad (4)$$

This equation is derived for structures where the S' module is considered as BS. When the L' module instead is taken as BS, the formula becomes:

$$\Delta d/d_N^* = 2ti/(N + 2). \quad (5)$$

Equations 4 and 5 are valid only for sequences where $L' = 1$ or $S' = 1$, respectively. It should be also noted that they are not applicable to the derivation of Bi_2Te_3 from BiTe_{ccp} since the latter

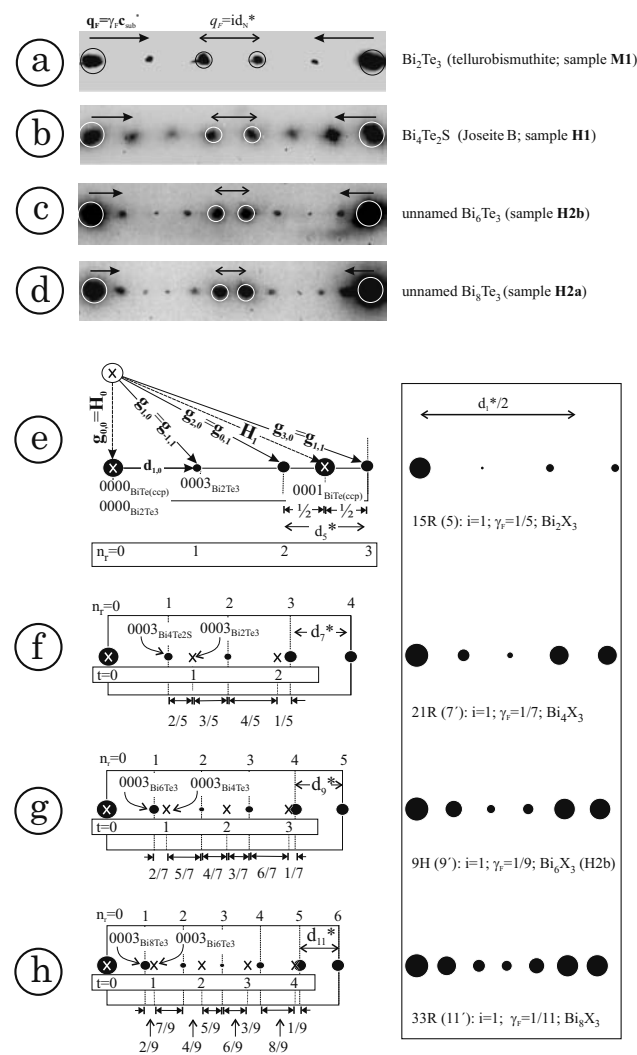


FIGURE 9. (a–d) Observed distribution of superstructure reflections and their intensities within d_1^* interval along $(000l)$ central rows of EDPs in Figures 5a–5d [structures built by a single type of Bi_{2k}X_3 module ($k = 1-4$; $i = 1$)]. They show the variation of \mathbf{q}_F with composition (decreasing with increasing Bi content) and the distance between the pair of brightest reflections about the center of d_1^* that is $q_F = id_N^*$. (e–h) Derivation of stacking sequences for phases in a–d using the fractional shift method of Van Landuyt et al. (1970) for interface modulated structures (DS, circles) relative to a basic structure (BS, crosses), done by overlapping the two corresponding DS and BS patterns. Fractional shifts shown below each pattern. Indexation with respect to hexagonal setting ($hklm$). Right inset gives patterns for the same stacking sequences as represented on the left but with intensities drawn proportional to values calculated in Table 3, thus showing a precise relative variation in intensity of reflections. In e, the reciprocal lattice vector ($\mathbf{g}_{t,m}$) describing the superstructure reflections is shown for Bi_2Te_3 (DS) relative to BiTe_{ccp} (BS). In f–h, each DS pattern is derived from the one above considered as BS.

¹ Deposit item AM-09-012, Appendix A with Appendix Tables and Appendix B, information about the MSCG for the simulation program. Deposit items are available two ways: For a paper copy contact the Business Office of the Mineralogical Society of America (see inside front cover of recent issue) for price information. For an electronic copy visit the MSA web site at <http://www.minsocam.org>, go to the American Mineralogist Contents, find the table of contents for the specific volume/issue wanted, and then click on the deposit link there.

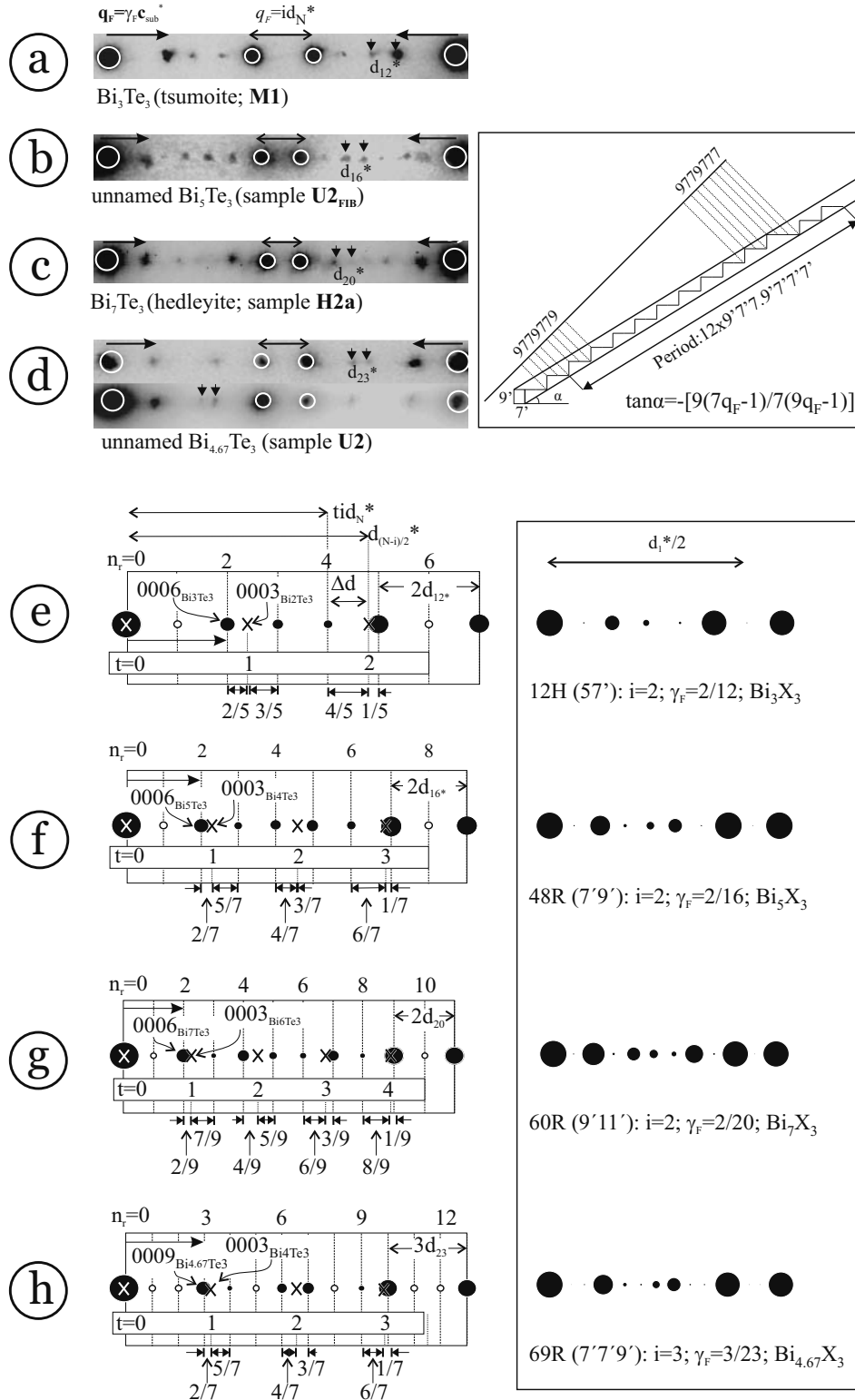


FIGURE 10. (a–d) Observed distribution of superstructure reflections and their intensities within d_1^* (hexagonal subcell) interval along (000) central rows of EDPs in Figures 5e, 5h, 5g, and 5f (structures built by two types of Bi_{2i}X_3 modules; $i \neq 1$). They show the variation of \mathbf{q}_F with composition (decreasing with increasing Bi content) and the distance between the pair of brightest reflections about the center of d_1^* that is $q_F = id_N^*$. (e–h) Derivation of stacking sequences for phases in a–d (see caption to Fig. 9). In e–h, the BS is chosen using id_N measurements (see text). In e, the segments used to calculate Δd are shown. The upper-right inset shows the derivation of stacking sequence for the structure in h using the measured value of \mathbf{q}_F and the strip method of Frangis et al. (1990).

is not part of the homologous group considered here. Calculations of all fractional shifts for all the investigated structures are given in Table A2 Appendix A¹. Introducing these values in Equation 2 we obtain the displacements ($m\mathbf{H}_i \cdot \mathbf{R}$) for half the number of reflections across the d_1^* interval (the other half is a mirror image) for each structure (Tables A3–A8 in Appendix A). The calculated values correspond to the measured fractional shifts as indicated on Figures 9e–9h and 10e–10h.

The observed intensity variation in the patterns, as well as the absence of some reflections, can be explained if we consider the intensity of each reflection to be proportional to the equation obtained from the potential function $V_g = V_H \sin(\pi u d) / \pi u d$:

$$\sin^2[\pi(m - \mathbf{HR})] / [\pi(m - \mathbf{HR})]^2 \tag{6}$$

where $u = (1/d)(m - \mathbf{HR})$ (Van Landuyt et al. 1970). Using the shift values, it is thus possible to calculate the relative intensities at all (m, t) conditions (Tables A3–A8 in Appendix A¹). The intensity at a given n_r position is the sum of all contributions from all BS reflections. It can be seen, however, that for $m > 1$, the intensity contribution from a given t is at least an order of magnitude weaker than that for $m = 0$. This allows us to consider as relevant only those contributions from the nearest BS reflections for a given n_r . The expected diffraction pattern can then be drawn proportionally to the calculated intensity values (Table 3; Figs. 9 and 10, insets) and compared with the observed patterns (Figs. 9e–9h, 10e–10h). The missing reflections in those structures composed of two module types can now be seen to have intensities an order of magnitude lower than the observed reflections.

Other effects such as different types of atoms in the same

structural arrangement can also affect the observed intensities. For example, the missing reflections predicted by calculation for 57' using the basic structure 5 (Table A6, Appendix A¹; Fig. 10e) are observable if the structure is doped with Ge (e.g., structure 12H = 57 shown in Fig. 3c in Frangis et al. 1990). We note that this is not observed when Se instead of Te is present in this structure, e.g., compare Figure 3g in Frangis et al. (1990) with our Figure 10e.

POLYSOMATISM

Minimal shift condition

The above results show that the shift condition that must be considered for a pattern to have the brightest two reflections located about the middle of d_1^* always separated by id_N^* is: $\Delta d = 1/N_b$, (N_b is the number of layers in the basic structure). We call this the “minimal shift condition” (MSC) since $1/N_b$ is the smallest rational fraction that can be obtained for a given basic structure.

Knowing that homology in the group relates the two building modules, S' and L' , by the k number, and $i = S' + L'$, a program (MSCG, Appendix B¹) was compiled to check this condition for any structure for which S', L' , and k are known. The MSCG program calculates the intensities for all reflections within the d_1^* interval and iterates such calculations for all possible substructures, finding those that obey the MSC as solutions for the basic structure (see introductory text to MSCG, Appendix B¹). The numerical simulation for intensities within d_1^* can be compared with the observations thus constraining the stacking sequence estimated from a diffraction pattern. The example below illustrates the applicability and necessity of this method.

TABLE 3. Sum of $I_{(m,t)}$ intensities for $(N - i)/2$ reflections at position n_r (see Fig. 10), calculated for all the types of analyzed structures (Appendix A¹, Tables A1, A3–A9¹), using the fractional shift method of van Landuyt et al. (1970)

BS	Analytical values									Computed value
	BiTe _{ccp} na	Bi ₂ X ₃ 5	Bi ₄ X ₃ 7'	Bi ₆ X ₃ 9'	Bi ₈ X ₃ 11'	Bi ₁₀ X ₃ 13'	Bi ₁₂ X ₃ 15'	Bi ₁₄ X ₃ 17'	Bi ₁₆ X ₃ 19'	
DS	Bi ₂ X ₃ 5	Bi ₄ X ₃ 9'	Bi ₆ X ₃ 13'	Bi ₈ X ₃ 17'	Bi ₁₀ X ₃ 21'	Bi ₁₂ X ₃ 25'	Bi ₁₄ X ₃ 29'	Bi ₁₆ X ₃ 33'	Bi ₁₈ X ₃ 37'	Bi ₂₀ X ₃ 41'
i (DS)	1	1	1	1	2	2	2	3	3	4
N	5	7	9	11	12	16	20	23	23	306
N _b	na	5	7	9	5	7	9	7 (low)	16 (high)	23
Intensity (n_r) = $\sum I_{(m,t)}$										
$n_r = 0$	1.0162	1.0512	1.0533	1.0506	1.0174	1.0169	1.0153	1.0082	1.0580	$n_r = 0$ 1.0006
1	0.0450	0.5836	0.8000	0.9063	0.0492	0.0456	0.0389	0.0152	0.5267	13 0.7307
2	0.4053	0.3093	0.4219	0.5955	0.5773	0.7741	0.8679	0.0424	0.3500	27 0.5881
3	0.4053	0.9109	0.5714	0.5059	0.2654	0.1617	0.1223	0.7666	1.0447	40 0.9764
4		0.0243	0.9902	0.7450	0.0905	0.3183	0.5219	0.1365	0.7715	53 0.8548
5			0.0146	1.0208	0.8887	0.5383	0.3519	0.0609	0.2673	66 0.3711
6				0.0096	0.0314	0.0776	0.2159	0.3046	0.8826	67 0.4415
7					0.0072	0.9538	0.7041	0.5311	0.9775	80 0.9054
8						0.0247	0.0668	0.0555	0.3006	93 0.9463
9						0.0042	0.9796	0.0442	0.6604	106 0.5144
10							0.0203	0.9442	1.0972	107 0.3047
11							0.0206	0.4454		120 0.7961
12								0.0082	0.4454	133 0.9949
13								0.0019	1.0972	146 0.6610
										160 0.6610
										173 0.9949

Notes: All values >0.1 are given in bold. BS = basic Structure; DS = Derived Structure; $i = S' + L'$, where S' is the number of short ($Bi_{2k}X_3$) modules and L' is the number of long ($Bi_{2(k+1)}X_3$) modules; N = number of total layers in the structure. X = Te, Se, S; na: not applicable. Italics: sum of intensities for the first reflection situated after the middle of d_1^* interval considering the contribution of H_i vectors from the left side of this interval.

All the stacking sequences interpreted from the EDPs are consistent with the lattice images obtained (Figs. 6 and 8), except the structure 7'7'9' (TEM sample U2). In this case, the fringes show polysomatic disorder, i.e., intergrowths of two sequences P1: 7'7'9' and P2: 7'7'7'9', with variable periodicities; P1 appears

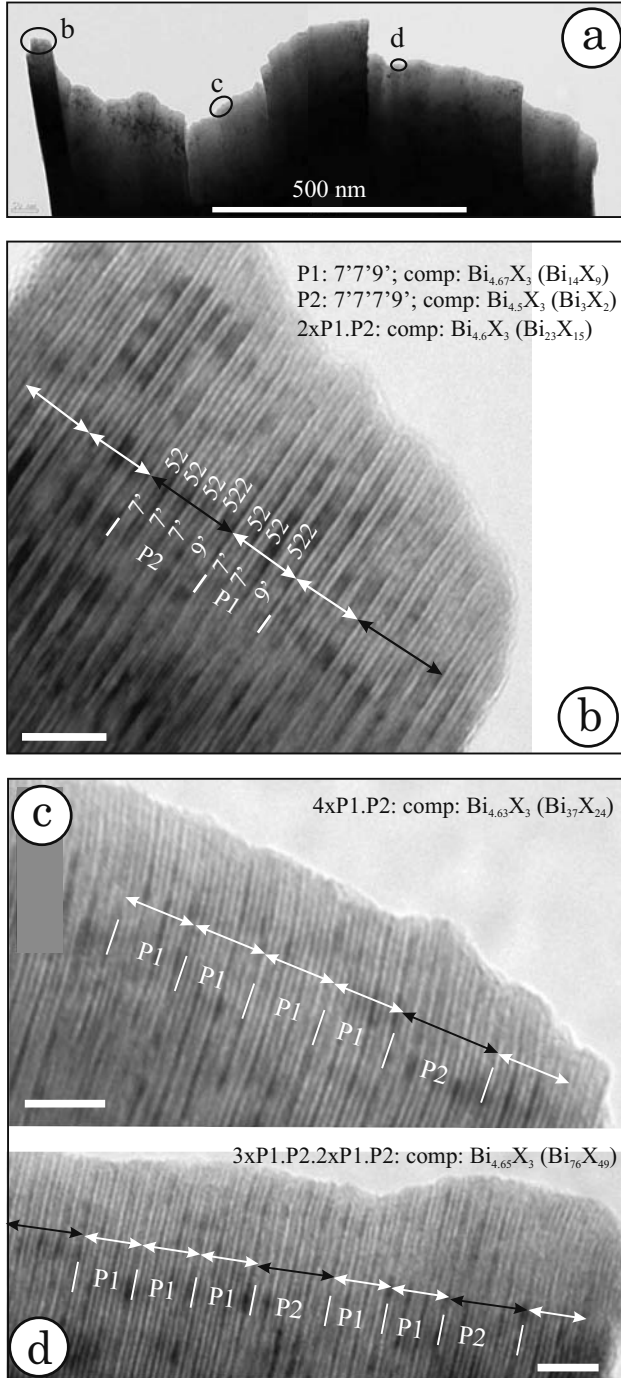


FIGURE 11. HRTEM images showing polysomatic disorder in fringes along the edge of a grain for which EDP (Fig. 5f) and interpretation of 7'7'9' structure (Fig. 10h) were obtained (sample U2). (b–d) Positions marked on along the edge as in a, the sequences show two types of polysomes with variable repeats as indicated; calculated compositions are also given. Scale bars: 5 nm.

more frequently (Fig. 11). To check whether the structure is indeed the P1 structure as calculated from measuring d_N^* , we also tried the “strip” method of Frangis et al. (1990). Measuring the \mathbf{q}_F vector on the diffraction image, which is a longer segment than d_N^* , and thus presumably carries a smaller measurement error, it is then possible to estimate a much longer sequence ($12 \times P1.P2$), where $N = 306$, $i = 40$, $S' = 27$, and $L' = 13$ (Fig. 10d, right side).

Numerical simulations of the patterns expected for $12 \times P1.P2$ when considering either 7' or P1 as a basic structure show only P1 as a solution. However, in this case, the number of reflections with intensities higher than 0.1 is much greater (in excess of $N_b = 23$, which is the number of layers for P1; Table 3) than that observed. Instead, simulation of 7'7'9' with base 7' reproduced the number of reflections, as well as relative intensities observed (Table 3). We thus conclude that our structure is closer to a 7'7'9' sequence rather than to $12 \times P1.P2$, despite the notable range of polysomatic disorder observed from the fringes (Fig. 11), which is reflected only as an elongation of the reflections observed in some of the diffractions for our structure.

ORDERED POLYSOMES AS STRUCTURAL BLOCKS

From all the structures discussed here it appears that the MSC is always respected if the stacking sequence is composed of two types of blocks, one of which is repeated only once. This means that for a given number of $S'(Bi_{2k}X_3)$ and $L'[Bi_{2(k+1)}X_3]$ modules, two polysomes (larger blocks formed by ordered sequences of the two types of modules) can be arranged so that one of them is a subsequence of the other (see example below). The polysome with the higher number of repeats in the entire sequence can be considered as the basic structure. It can be shown by simulation that there will always be only two solutions for N_b of the basic structure that satisfy the minimal shift condition. The two are not independent, however, since the sum of the two values obtained for N_b is equal to N of the entire sequence. In general, for $i > 2$, considering the basic structure with the smaller N_b will reproduce the observed pattern more accurately. For example, for structure 7'7'9', taking the larger $N_b = 16$ (7'9') will result in a pattern with more reflections than actually observed (Table 3). For $i = 1$ or 2, however, the basic structure with the larger N_b can sometimes give a better prediction of the pattern, e.g., the Ge-doped structure 57 in Figure 3c from Frangis et al. (1990), which shows all 11 superstructure reflections that would be obtained when $N_b = 7$.

The following example illustrates how the MSC can be used to reduce the number of possible stacking sequences for a given composition. Taking $S' = 8$ and $L' = 5$ for $k = 1$ (i.e., using 5 and 7' modules), the simulation gives $N_b = 29$. This number represents a polysome in which there are 3×5 and $2 \times 7'$ modules. The number of ways to arrange these modules (5 and 7') is $5!/(3!2!) = 10$. After comparing the ten variants, only two were found to represent different stacking sequences: 5557'7' and 557'57'. From these basic stacking sequences we can obtain two derived structures as follows: 5557'7'.5557'7'.557' and 557'57'.557'57'.557' by extracting a 57' sequence from each third unit cell of the basic structure. According to the model above we would expect that both structures have the same diffraction pattern (they are polytypes) and the actual stacking sequence can

only be found from lattice fringes. The value of this prediction can be seen if we consider that the number of possible stacking combinations for this compound would have otherwise been very large [i.e., $13!/(8!5!) = 1287$ even though many of these would be equivalent].

Predictions and constraints on the homology in the tetradymite group

As shown here, both the \mathbf{q} and \mathbf{q}_F vectors underpin structural modulations that relate chemical changes from one phase to another and describe a similar trend of variation: a monotonic decrease of modulations with increase in Bi. The subcell (~ 0.57 nm) obtained by the 4D displacive model is $3\times$ longer than the average interlayer $d_1 \sim 0.2$ nm representing $c/3$ of the basic subcell in the 3D displacement model.

The position of \mathbf{q} prime (onto one of the two brightest reflections about the middle of the d_1^* interval) is always easy to observe on diffractions and thus the 4D indexing system is preferable. The 3D model for \mathbf{q}_F , adapted here to include the homology between the Bi_{2k}X_3 modules and the “minimal shift condition,” can be used not only to identify, but also to predict, stacking sequences for any composition. This allows for discrimination between polysomatic sequences corresponding to single phases in the group and those that are random. The “minimal shift condition” imposed on polysomatism as required by the model adds a hierarchical level of homology to the group: certain combinations of simple Bi_{2k}X_3 modules form larger building blocks. The same model applies to the chalcogen-rich series since the Bi_{2k}X_3 and M_pX_{p+1} modules are equivalent for any $k = p - 1$.

Incommensurability has a different significance in the two models. In the 4D model, the “incommensurate periodicities” along the homoatomic arrays (leading to variation in the measured atomic positions in the same structure; Lind and Lidin 2003) are inherent to all the structures built by two types of modules. However, the effect this has on the general pattern obtained by electron diffraction is not measurable and thus can be ignored for the purpose of identifying the stacking sequences. All the diffractions obtained here for such phases are commensurate, even in the case where polysomatic disorder is notable—as seen for structure $7'7'9'$.

In the 3D model, a consequence of the fact that fulfillment of the MSC requires polysomatism for certain Bi/X ratios is that incommensurability (aperiodic structures) should be predictable for the longer and/or highly disordered polysomes. Sequences formed by more than two types of Bi_{2k}X_3 modules (e.g., $11'9'55$, $11'9'7'$), or two Bi_{2k}X_3 modules that do not have consecutive k (e.g., $11'55$), are polysomatic intergrowths of different phases. It can be assumed that their diffraction would be incommensurate as well, whether the intergrowths are ordered or disordered. However, the check for MSC should indicate whether the incommensurability observed on a given diffraction pattern relates to random intergrowths or, alternatively, one of the longer polysomes represents a single-phase in the group.

Although the structural formula $n\text{Bi}_2 \cdot m\text{Bi}_2\text{X}_3$ constrains the internal configuration of Bi_{2k}X_3 modules by the relation $n/m = k - 1$, it does not explicitly show the homology for phases with $n/m > 1$. In particular it does not constrain the fact that the only way in which adjacent 5 (Bi_2X_3) units can occur in a sequence

representing a single-phase is when they combine with 2 (Bi_2) units to form repeats corresponding to only two Bi_{2k}X_3 modules with consecutive k . For example, for $n = 5$ and $m = 4$, the sequence $225.25.25.25 = 9'7'7'7'$ corresponds to a single phase whereas $2225.522.55 = 11'.9'.55$ does not. Both sequences give, however, the same composition (Bi_3X_2).

Genetic considerations

Recognizing which of the stacking sequences correspond to single phases is important for assessing equilibrium diagrams, e.g., for the systems Bi-Te or Bi-Se (Okamoto and Tanner 1990; Okamoto 1994), as much as for petrogenetic interpretations. Slower cooling rates, of advantage when studying mixed layer compounds where stabilization of certain stacking sequences is dependent upon time, are inherent to specific geologic environments. For example, the richest Bi-phase obtained experimentally in the system Bi-Te is Bi_7Te_3 , whereas the results here predict the existence of Bi_8Te_3 , a phase still richer in Bi and not previously identified. The skarn deposits at the Good Hope Mine, Hedley, from which the sample (**H2a**) originates is formed in a deep environment, thus increasing the efficiency of slow cooling rates in stabilizing Bi-rich phases.

The laboratory results are nonetheless paralleled by the fact that the mineral corresponding to Bi_7Te_3 , hedleyite, is relatively common, whereas the nearest phases with $i = 1$, i.e., Bi_2Te ($=\text{Bi}_6\text{Te}_3$) and Bi_8Te_3 , are unnamed species, only occasionally reported (or inferred) from EPMA data (e.g., Cook et al. 2007a). This is despite the fact that both Bi_2Te and Bi_8Te_3 have simpler stacking sequences (mods $9'$ and $11'$, respectively) than Bi_7Te_3 ($i = 2$; $9'11'$) and should, presumably, be more stable. Why then are Bi_2Te and Bi_8Te_3 not more widely reported? Small chemical differences between Bi_7Te_3 and either Bi_2Te or Bi_8Te_3 (3 at% or 2 wt% Te) may make them difficult to recognize on the scale of the microprobe beam. In any case, inhomogeneous material, containing intergrowths of Bi_2Te , Bi_8Te_3 and Bi_7Te_3 will inevitably give a “bulk” composition approximating Bi_7Te_3 . In fact, Cook et al. (2007a) noted that the variety of published microanalytical data for hedleyite reflected a broad field from Bi_6Te_3 to Bi_8Te_3 (or even Bi_9Te_3). Small chemical variations can be assumed to occur at a local scale during crystallization. For example, in mixed-layer compounds, often occurring as lamellae stratified along c in a given package, compositional variation can be recognized from one lamella to another, e.g., hedleyite lamellae embedded within a patch of Bi_8Te_3 cut across the stratification (Fig. 4c). The inner part of the patch in sample **H2a** from which the TEM samples were prepared would give a bulk composition midway between Bi_7Te_3 and Bi_8Te_3 (Fig. 12) if the EPMA data obtained from profiles along and across the lamellar package were averaged (Fig. 4c; Table 2).

The effect of compositional variation across interstratified lamellar packages has to be assumed for sample **U2** since the two phases identified from TEM samples prepared from the same patch, i.e., **U2**: $\text{Bi}_{14}\text{Te}_9$ ($=\text{Bi}_{6.66}\text{Te}_3$) and **U2_{FIB}**: Bi_5Te_3 , are different from the one expected from EPMA, i.e., $\text{Bi}_{17}\text{Te}_{12}$ ($=\text{Bi}_{4.25}\text{Te}_3$) (Fig. 12). This compositional difference is too high to be attributed to EPMA analytical error. The sequence $2 \times (7'7'9').7'7'7'9'$ ($\text{Bi}_{23}\text{Te}_{15} = \text{Bi}_{4.6}\text{Te}_3$; Fig. 11b) observed among the polysomes at the edge of the grain in Figure 11a indicates that

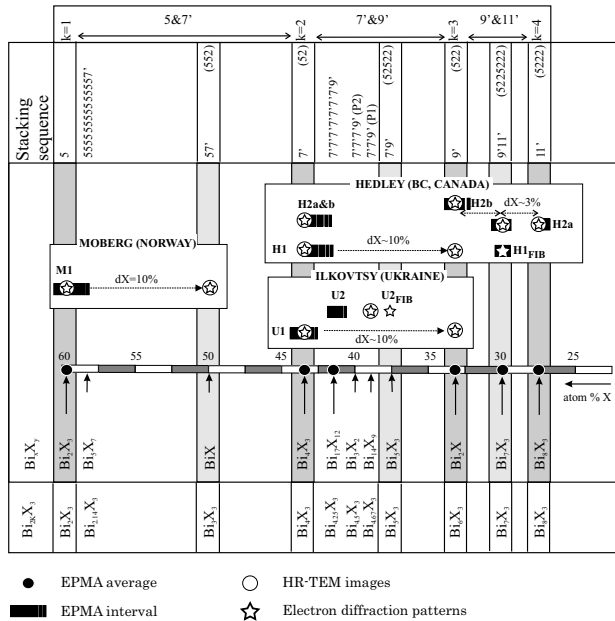


FIGURE 12. The compositional ranges for structures in single samples confirmed by HRTEM (as much as ~10 at% X) are compared with the ranges of compositions inferred by EPMA. Besides the phase corresponding to the average EPMA composition (in the majority of cases), a minority of grains investigated by HRTEM correspond to phases well beyond the limits of the EPMA data, for example, BiX (sample **M1**) and unnamed Bi₂X (samples **U1** and **H1**).

the overall composition of this grain is metal-deficient relative to the composition inferred by the stacking sequence 7'7'9' (Bi₁₄Te₉ = Bi_{6.67}Te₃). The volcanic environment at Ilkovtsy provides for rapid cooling rates, converging on laboratory conditions. Both polysomatic disorder and formation of intermediate phases (with EPMA-scale compositions between two Bi_{2k}X₃ phases with consecutive k,) is thus predictable within and across interstratified lamellar packages where the Bi_{2k}X₃, Bi_{2(k+1)}X₃ phases are not necessarily found for k < 3.

In three cases (**M1**, **U1**, **H1**), the variation in Bi/X seen in the EPMA data, although indicative of some lattice-scale inhomogeneity (Figs. 4e and 4f), do not cover all those compositions inferred from the HRTEM investigation. Besides the phase corresponding to the average EPMA composition (in the majority of cases), a minority of grains investigated by HRTEM correspond to phases with stoichiometry well beyond the limits of the EPMA data—for example, BiX (sample **M1**) and unnamed Bi₂X (samples **U1** and **H1**). Although the composition of these phases cannot be precisely estimated [it may be either BiTe or Bi(Te,S) in **M1**], their stacking sequences are simpler than those of the phases neighboring the main component in each sample, e.g., 57' (i = 2) for BiX instead of 13 × (5), 7' (i = 14) for Bi₅X₇ in **M1** (Fig. 12). The compositional ranges for structures in single samples confirmed by HRTEM (as much as ~10 at% X) are compared with the ranges of compositions inferred by EPMA in Figure 12. At Moberg (**M1**), it is possible to suggest that for-

mation of a 57 structure (M₅X₇) would have been favored if Pb had been available. The observations would appear to indicate that the small metal excess measured for the Bi_{2k}X₃ phases with k = 1, 2 attract nucleation of nano-scale inclusions that have a higher Bi/X ratio than might be expected from the corresponding EPMA data. Two-phase separation triggered by exsolution might be invoked in this case.

ACKNOWLEDGMENTS

C.L.C. acknowledges receipt of an Australian Research Council "Discovery" grant. C.L.C. also thanks the Nanostructural Analysis Network Organization for access to the dual-beam focused ion beam at University of New South Wales, Sydney. We acknowledge Sergey Bondarenko and Alexander Grinchenko (Ukrainian Transcarpathians) and Bill Howard (Hedley material) for their kind assistance with sample material and with discussion. Discussion with Ray Withers also helped C.L.C. during the course of the research. This study is a contribution to International Geoscience Program (IGCP) Project 486 "Gold-telluride deposits." The manuscript benefited considerably from the insightful comments of reviewers Emil Makovicky and Péter Németh.

REFERENCES CITED

- Agafonov, V., Rodier, N., Céolin, R., Bellissent, R., Bergman, C., and Gaspard, J.P. (1991) Structure of Sb₂Te. *Acta Crystallographica*, C47, 1141–1143.
- Amelinckx, S., Van Tendeloo, G., Van Dyck, D., and Van Landuyt, J. (1989) The study of modulated structures, mixed layer polytypes and 1-D quasi-crystals by means of electron microscopy and electron diffraction. *Phase Transitions*, 16/17, 3–40.
- Cook, N.J., Ciobanu, C.L., Wagner, T., and Stanley, C.J. (2007a) Minerals of the system Bi-Te-Se-S related to the tetradymite archetype: Review of classification and compositional variation. *Canadian Mineralogist*, 45, 665–708.
- Cook, N.J., Ciobanu, C.L., Stanley, C.J., Paar, W., and Sundblad, K. (2007b) Compositional data for Pb-Bi tellurosulphides. *Canadian Mineralogist*, 45, 417–435.
- Frangis, N., Kuypers, S., Manolikas, C., Van Tendeloo, G., and Amelinckx, S. (1990) Continuous series of one-dimensional structures in compounds based on M₂X₃ (M = Sb, Bi, X = Se, Te). *Journal of Solid State Chemistry*, 84, 314–334.
- Gaudin, E., Jobic, S., Evain, M., Brec, R., and Rouxel, J. (1995) Charge balance in some Bi₂Se₃ phases through atomic structure determination and band structure calculations. *Materials Research Bulletin*, 30, 549–561.
- Imamov, R.M. and Semiletov, S.A. (1971) The crystal structure of the phases in the systems Bi-Se, Bi-Te, and Sb-Te. *Soviet Physics—Crystallography*, 15, 845–850.
- Lima de Faria, J., Hellner, E., Makovicky, E., and Parthe, E. (1990) Nomenclature of inorganic structure types. Report of the International Union of Crystallography Commission on Crystallographic Nomenclature Subcommittee on the Nomenclature of Inorganic Structure Types. *Acta Crystallographica*, A46, 1–11.
- Lind, H. and Lidin, S. (2003) A general structure model for Bi-Se phases using a superspace formalism. *Solid State Sciences*, 5, 47–57.
- Makovicky, E. (1997) Modular crystal chemistry of sulphosalts and other complex sulphides. In S. Merlino, Ed., *Modular Aspects of Minerals*, 1, p. 237–271. EMU Notes in Mineralogy, Eötvös University Press, Budapest.
- Okamoto, K. (1994) The Bi-Se (bismuth-selenium) system. *Journal of Phase Equilibria*, 15, 195–201.
- Okamoto, K. and Tanner, L.E. (1990) Bi-Te (Bismuth-Tellurium). In T.B. Massalski and K. Ohamoto, Eds., *Binary Alloy Phase Diagrams*, p. 800–801. ASM International, Materials Park, Ohio.
- Shelimova, L.E., Karpinsky, O.G., Kosyakov, V.I., Shestakov, V.A., Zemskov, V.S., and Kuznetsov, F.A. (2000) Homologous series of layered tetradymite-like compounds in Bi-Te and GeTe-Bi₂Te₃ systems. *Journal of Structural Chemistry*, 41, 81–87.
- van Landuyt, J., De Ridder, R., Gevers, R., and Amelinckx, S. (1970) Diffraction effects due to shear structures: A new method for determining the shear vector. *Materials Research Bulletin*, 5, 353–362.

MANUSCRIPT RECEIVED DECEMBER 23, 2007

MANUSCRIPT ACCEPTED NOVEMBER 6, 2008

MANUSCRIPT HANDLED BY LAURENCE GARVIE